# FABRICATION AND CHARACTERIZATION OF MICROELECTROMECHANICAL RESONATORS

A THESIS
SUBMITTED TO THE DEPARTMENT OF PHYSICS
AND THE INSTITUTE OF ENGINEERING AND SCIENCE
OF BILKENT UNIVERSITY
IN PARTIAL FULFILLMENT OF THE REQUIREMENTS
FOR THE DEGREE OF
MASTER OF SCIENCE

By
Sevil Özer
January, 2006

I certify that I have read this thesis and that in my opinion it is fully adequate, in scope and in quality, as a thesis for the degree of Master of Science.

Assoc. Prof. Dr. Recai Ellialtıoğlu (Supervisor)

I certify that I have read this thesis and that in my opinion it is fully adequate, in scope and in quality, as a thesis for the degree of Master of Science.

Dr. Tarık Reyhan (Co-Supervisor)

I certify that I have read this thesis and that in my opinion it is fully adequate, in scope and in quality, as a thesis for the degree of Master of Science.

Assoc. Prof. Dr. Ahmet Oral

Approved for the Institute of Engineering and Science:

Prof. Dr. Mehmet B. Baray
Director of the Institute Engineering and Science

# ABSTRACT

# FABRICATION AND CHARACTERIZATION OF MICROELECTROMECHANICAL RESONATORS

Sevil Özer
M.S. in Physics
Supervisors: Assoc. Prof. Dr. Recai Ellialtıoğlu and
Dr. Tarık Reyhan
January, 2006

Micromachined mechanical resonators are of considerable interest because of their many important scientific and technological applications. They can be used as a components of radio-frequency filters in communication systems, mechanical electrometer or magnetometer for sensitive detection of force, charge, pressure.

This work is directed towards the fabrication and characterization of microelectromechanical resonators, cantilevers and bridges. The SOI cantilever and the silicon nitride cantilevers and bridges are fabricated by using surface micromachining techniques. They are fabricated in the Advanced Research Laboratory of Bilkent University. The center frequencies are ranging from 20 kHz to 270 kHz. The characterization of cantilevers and bridges are done by using the beam deflection method and the fiber optic interferometer method. The dynamic response of the first devices, such as the resonance frequencies and the quality factors will be reported. In addition, simple beam theory and some fundamental loss mechanisms will be discussed. The experimental results will also be compared with the theoretical ones.

*Keywords:* Resonators, Cantilever, Bridge, Quality Factor, Laser Beam Deflection, Fiber Optic Interferometer.

# ÖZET

## MİKROMETRE BOYUTLARDA ÜRETİLMİŞ MEKANİK ÇINLAÇLARIN ÜRETİM VE KARAKTERİZASYONU

Sevil Özer
Fizik, Yüksek Lisans
Tez Yöneticileri: Doç. Dr. Recai Ellialtıoğlu ve
Dr. Tarık Reyhan
Ocak, 2006

Mikrometre boyutlarda üretilmiş mekanik çınlaçlar günümüzde bilim ve teknolojideki önemli uygulamalarından dolayı oldukça ilgi görmektedir. Bu çınlaçlar kuvvetteki, yükteki ya da basınçdaki değişimi ölçmek için elektometrelerde ve magnetometrelerde kullanılır. Ayrıca mikro-çınlaçlar radyo-frekans süzgecinin bir parçası olarak da iletişim alanında kullanılmaktadır.

Bu çalışma, mikron boyutlarda yapılmış çınlaçların üretim ve karakterizasyonu amacıyla yürütülmüştür. Yalıtkan alttaş üzerine yapılandırılmış silisyum ve silisyum nitrat yapısındaki çınlaçlar, yüzeyde mikron boyutlarda üretilmiştir. Çınlaçların üretimi Bilkent Üniversitesi İleri Araştırma Laboratuvarında yapılmıştır. Çınlaçların karakterizasyonu ise iki değişik yöntem kullanılarak yapılmıştır. Karakterizasyonda bulunan sonuçlar daha sonra kiriş kuramı (beam theory) ile bulunan sonuçlarla karşılaştırılmıştır.

*Anahtar sözcükler*: Çınlaçlar, Dirsek, Köprü, ,Kalite Faktörü, Lazer Kiriş Sapması, Fiber optik Girişimölçeri.

# Acknowledgement

I am indebted to Assoc. Prof. Dr. Recai Ellialtıoğlu for constant help, support and encouragement as a supervisor during my MS work.

I also owe to special thanks to Dr. Tarık Reyhan and Assoc. Prof. Ahmet Oral for their helps, their valuable remarks on the problems during experiment and supplying me the experimental tools.

I would like to thank Dr. Aykutlu Dâna, Mehrdad Atabak and Aşkın Kocabaş for improving my knowledge and their great effort to explain things.

I am also grateful to my colleagues Bahar Kop, Münir Dede, Koray Ürkmen and Selcen Aytekin for their friendship and endless help during my thesis work.

Personally, I would like to thank Sinem Binicioğlu Çetiner, Barış Öztop, Engin Durgun, Deniz Çakır, Onur Umucalılar, Dündar Yılmaz, Kerim Savran, Cem Sevik and Emre Taşgın for their friendship during my graduate study.

I dept special thanks to Rasim Volga Ovalı for his friendly attitudes, remarkable help and motivation.

I also would like to express my special thanks to my parents Sabri and Emine Özer, my second family Sinan, Suna and Ogüncan Özer, my old brother Yahya Özer and my twin Soner Özer. They have always been with me and I consider myself most fortunate.

# Contents

1 INTRODUCTION 1

2 THEORETICAL BACKGROUND 4

2.1 Deflection of a Beam . . . . . 6

2.2 The Quality factor of a beam . . . . . 13

2.3 Loss mechanisms . . . . . 15

2.3.1 Air-damping effect . . . . . 15

2.3.2 Surface-related effects . . . . . 18

2.3.3 Clamping-Anchor losses . . . . . 19

2.3.4 Internal losses . . . . . 19

3 DEVICE FABRICATION 21

3.1 Cleaning . . . . . 22

3.2 Photolithography . . . . . 22

3.3 Etching . . . . . 25

3.4 Deposition . . . . . 28

3.5 Metallization . . . . . . . . . . . . . . . . . . . . . . . . . . . . 29

**4 BEAM CHARACTERIZATION AND ANALYSIS 32**

4.1 Fiber Optic Interferometer Technique . . . . . . . . . . . . . . . . . . 32

4.2 Fiber Optic Interferometric Measurement Results . . . . . . . . . . 38

4.3 Beam Deflection Atomic Force Microscopy . . . . . . . . . . . . . . 41

4.4 Beam Deflection Atomic Force Microscopy Results . . . . . . . . . 45

**5 CONCLUSION 49**

# List of Figures

2.1 Cantilever beams in fundamental *(a)* flexural, *(b)* torsional and *(c)* longitudinal vibration modes. . . . . . . . . . . . . . . . . . . . . . 4

2.2 Schematics of the fundamental vibration and its first two overtones of a flexural cantilever beam. . . . . . . . . . . . . . . . . . . . . . . 5

2.3 The first three bending modes of doubly clamped beam, i.e. bridge. 5

2.4 Strain in a cantilever . . . . . . . . . . . . . . . . . . . . . . . . . 7

2.5 The flexural behavior of a straight cantilever beam . . . . . . . . 8

2.6 The fabricated silicon nitride bridges. . . . . . . . . . . . . . . . . . 8

2.7 The fabricated silicon nitride cantilevers . . . . . . . . . . . . . . 13

2.8 Amplitude versus Frequency curve for a cantilever . . . . . . . . . 14

3.1 Photolithography process . . . . . . . . . . . . . . . . . . . . . . . 22

3.2 Comparison of negative and positive resists . . . . . . . . . . . . . 24

3.3 The exposure method: Contact mode . . . . . . . . . . . . . . . . . 25

3.4 Isotropic Wet Etching, the undercutting problem . . . . . . . . . 26

3.5 The undercutting problem in the fabrication of beam process . . . 27

3.6 Anisotropic Wet Etching . . . . . . . . . . . . . . . . . . . . . . . 28

3.7 Cantilevers etched by using the KOH solution from the back side of the SOI cantilevers . . . . . . . . . . . . . . . . . . . . . . . . 30

3.8 The fabricated silicon nitride bridges . . . . . . . . . . . . . . . . 31

3.9 The fabricated silicon nitride cantilevers . . . . . . . . . . . . . . 31

4.1 The connection scheme and the block diagram of the Fiber Optic Interferometric Technique . . . . . . . . . . . . . . . . . . . . . . . 33

4.2 The operation principle of the fiber optic interferometer . . . . . . 34

4.3 Interference signal versus cavity length . . . . . . . . . . . . . . . 36

4.4 Simplified circuit diagram for amplification of the interferometer photodiode current . . . . . . . . . . . . . . . . . . . . . . . . . . 37

4.5 The amplitude versus frequency graph of the both side suspended oscillator beam, bridge#1 . . . . . . . . . . . . . . . . . . . . . . . 39

4.6 The phase versus frequency graph of the both side suspended oscillator beam, bridge#1 . . . . . . . . . . . . . . . . . . . . . . . 39

4.7 The amplitude versus frequency graph of the both side suspended oscillator beam, bridge#2 . . . . . . . . . . . . . . . . . . . . . . . 40

4.8 The phase versus frequency graph of the both side suspended oscillator beam, bridge#2 . . . . . . . . . . . . . . . . . . . . . . . 40

4.9 The view of the beam deflection AFM set up from NanoSis [31]. . 42

4.10 The schematic representation of the approach set up for deflection detection of SOI cantilevers . . . . . . . . . . . . . . . . . . . . . 43

4.11 A quadrant phodetector . . . . . . . . . . . . . . . . . . . . . . . 44

4.12 The schematic description of the beam deflection set up . . . . . . 45
4.13 The measured resonance curve for SOI cantilever#1 . . . . . . . . . 47
4.14 The measured resonance curve for SOI cantilever#2 . . . . . . . . . 47
4.15 The measured resonance curve for SOI cantilever#3 . . . . . . . . . 48

# List of Tables

3.1 The growth of nitride film by using PECVD technique . . . . . . 29

4.1 The calculated and the measured values of the silicon nitride bridge and cantilevers . . . . . . . . . . . . . . . . . . . . . . . . . . . . . 38

4.2 The calculated and the measured parameters of the SOI cantilevers 46

4.3 Density and Young's Modulus for Siliconnitride and Silicon . . . . 46

# Chapter 1

# INTRODUCTION

Micromachined mechanical resonators, such as beams and diaphragms currently find their way in sensor research. The term microelectromechanical structures (MEMS) can be defined as the devices where the mechanical function is coupled to an electrical signal. MEMS technology has opened up a wide variety of applications such as communications (filters, relays, oscillators, optical swithes, LC passives), bio-medicine (immunoassays, microarrays for DNA detection, medical instrumentation, high throughput screening of drug targets), computer peripherals (memory, new I/O interfaces, read-write heads for magnetic disks), gas detection and mass flow detection [1].

A subgroup of MEMS are MEMS resonators. Micromachined mechanical resonators are of considerable interest because of their many important scientific and technological applications. They are used as components of radio-frequency filters in communication systems, mechanical electrometers or magnetometers for sensitive detection of charge, force, pressure, and acceleration [2]. Because of small dimensions of MEMS resonators, they are often able to achieve more precise measurements. Due to their small masses and feature sizes, MEMS sensors are able to detect extremely quantities, such as an adhesion of individual molecules to their surface. Another ability of the MEMS technology is that the mechanical elements of the sensor can be constructed on the same chip as the electrical circuits which are used to process changes in the mechanical elements. The ability of fabricating both mechanical and electrical components on the same chip can reduce the overall complexity of the device and the manufacturing process for fabricating device. This ability also leads to cost reduction in manufacturing of the devices.

Sensing functions can be accomplished by monitoring the change in resonant frequency due to either external force on the resonator or mass adsorption. The resonance frequency is the natural frequency of vibration determined by the physical parameters, including mass, tension or stiffness of the vibrating object. It also depends on the length, shape and the material of the resonator.

Atomic force microscopy can be given as an example of force sensor. As the force between the atoms of the tip and sample changes, the resonance frequency of the resonator also changes [3, 4]. Biological sensors work in a way that the resonator is coated with an immobilized antibody which can attract the certain type of molecules. This additional mass changes the resonant frequency of the resonator. MEMS gas sensors also work in a similar way. They are just coated with an active layer to absorb the certain gas molecules. That is resonant mass sensors operate by providing a frequency shift which is directly proportional to the inertial mass of the analyte molecules attracted onto the resonator [5] . Due to the small sizes of the microresonators, they are able to capture high frequency signals up to the magnitudes of $10^9$ Hz [6]. As the size decreases, NEMS mass sensing can provide significant advances in chemical and biological sensing and mass spectroscopy at the attogram scale [7].

Some type of resonators are beams (cantilevers, bridges, diagrams ), disks and comb-drives. Resonance frequency measurements provide useful insight into the repeability of MEMS manufacturing processes. Several techniques are available for making this measurement. These are optical beam deflection based on a laser diode focused at the free end of the cantilever, piezoresistance method based on the variation of the bulk resistivity with applied stress [8], piezoelelectric method, capacitance method based on the variation in capacitance between the cantilever and the fixed substrate [9].

This thesis is organized into five chapters. The first chapter provides an introduction to the work such as application areas. In the second chapter, the resonant frequency of the oscillator is examined by using the simple beam theory. This chapter also concentrates on the more general and the fundamental loss mechanism: such as air damping, anchor points, internal losses etc, are discussed. The third chapter provides a discussion on the microfabrication techniques used in the thesis. Each fabrication steps such as photolithography, the growth of the silicon nitride thin film etc. are explained in this chapter. Chapter four describes the characterization methods and the results obtained by using these methods. Finally, Chapter five outlines the conclusions and the discussions of this work.

# Chapter 2

# THEORETICAL BACKGROUND

This chapter focuses on the basic theory of vibration for single and double clamped beams, and the resonance parameters such as phase, amplitude, and Q-factor are explained briefly. These parameters can be determined if a frequency spectrum is obtained.

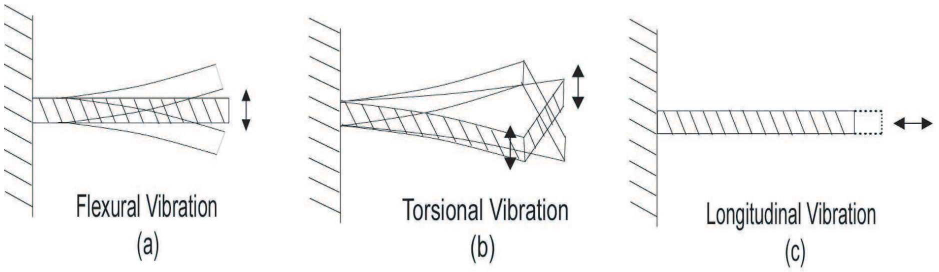

Figure 2.1: Cantilever beams in fundamental *(a)* flexural, *(b)* torsional and *(c)* longitudinal vibration modes.

A straight horizontal beams under a vertical force will deform. After this force is removed the beam will return to its original shape, but its inertia will keep the beam in motion. Then the beam will begin to vibrate with its characteristic frequencies. The structures, a beam, bridge, or diaphragm, have many different vibration modes and each mode has its own displacement pattern, resonance frequency and Q-factor [10]. The vibrational modes of a cantilever beam are shown in Figure 2.1. Morever, each mode can have many higher-order resonance frequencies, so called overtones or harmonics. In the case of a rectangular beam, many different resonance modes can exist, such as bending, twisting, expanding and contracting. Figure 2.2 and 2.3 show the first three bending modes of vibration of a single clamped beam [10] and a doubly-clamped beam [11], respectively. The cross-section of the beams studied in this thesis are long, thin rectangular beams (however, in reality, there may have been some deviations because of the wet etching processes). Figure 2.6 and 2.7 show the silicon nitride bridges and cantilevers fabricated during this work, respectively.

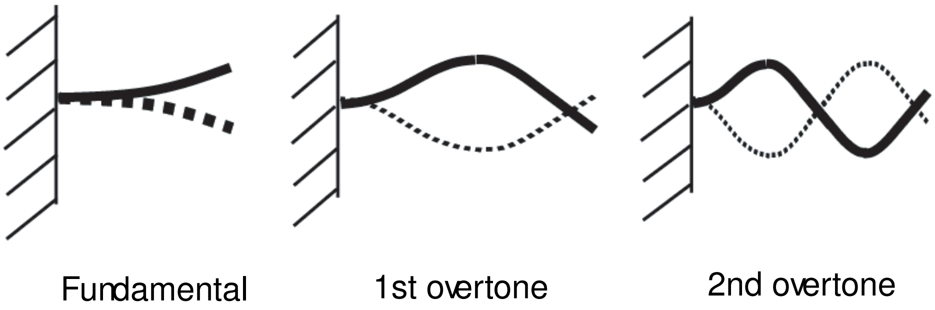

Figure 2.2: Schematics of the fundamental vibration and its first two overtones of a flexural cantilever beam.

The typical dimensions of single clamped beams microfabricated in this study, are L=240 $\mu m$, 180 $\mu m$, 140 $\mu m$ long for SOI, and 250 $\mu m$, 200 $\mu m$, 150 $\mu m$, and 100 $\mu m$ long for silicon nitride , w= 30 $\mu m$, 50 $\mu m$, and 100 $\mu m$ wide, and t= 2 $\mu m$ and 4 $\mu m$ thick, and that of double-clamped beams are L=100 $\mu m$, w= 5 $\mu m$, t= 0.5 $\mu m$. Since the quality factors of resonant sensor is also closely related to the mechanical properties of the resonator material, silicon has been chosen as the beam material. Silicon has good elasticity, high purity, and low levels of defects and dislocations [12]. Silicon is also an anisotropic material, it has different material properties in different crystallographic directions. It is usable for anisotropic etching for the three dimensional shaping of the microstructures.

Figure 2.3: The first three bending modes of doubly clamped beam, i.e. bridge.

## 2.1 Deflection of a Beam

The response of a resonant system to an external static loading or a static mass loading has been studied analytically in the literature, [13, 14] . Basic theory of vibration for single and double clamped beams is discussed in this section. This theory is restricted to a prismatic (equal cross section), homogeneous, straight and untwisted structure. The thickness ($t$) and the width ($w$) have to be small compared to the length ($L$), that reduces the problem to an one-dimensional problem along the length of the beam. Additionally, it is assumed that the normal stress ($\sigma$) in the $y$ and $z$ direction can be neglected [14]. A beam subjected to a point load will deflect and bend into a curve. If the load is increased, the deflection will be greater. To obtain the general equations for the deflection curve of a beam, we take the coordinates at the fixed end, with the $x$ axis directed to the right and the $y$ axis directed downward shown in Figure 2.4. We assume that the $xy$ plane is a plane of bending. The deflection of the at any point at distance $x$ from the origin is the displacement of that point in the $y$ direction, measured from the $x$ axis to the deflection curve. If the deflection of the beam is given by the displacement function $\nu$ in terms of location $x$, the equation of the deflection can be obtained. From the Figure 2.4, $rd\theta = ds$ where $r$ is the radius of curvature, hence, the curvature $\kappa$ is equal to the reciprocal of the radius of the curvature given by the following equation [15]

$$\kappa = \frac{1}{r} = \frac{d\theta}{ds} \tag{2.1}$$

The slope of the deflection curve is the first derivative of the displacement function known from calculus. The slope is equal to the tangent of the angle of rotation $\theta$, because $dx$ is infinitesimally small, thus

$$\frac{d\nu}{ds} = \tan\theta \tag{2.2}$$

or

$$\theta = \arctan\frac{d\nu}{ds} \tag{2.3}$$

Equations 2.1, 2.2 and 2.3 are based on the geometric considerations, thus, they can be applied to a beam of any material. Furthermore, there is no restriction on the magnitudes of the slopes and deflections.

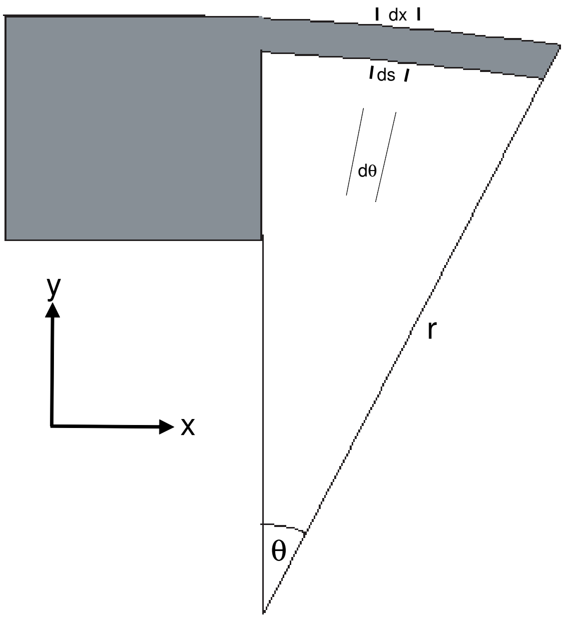

Figure 2.4: Strain in a cantilever

Most beams undergo only very small deflections when they are loaded. This results to the small curvatures. Under these conditions, the angle $\theta$ is a very small quantity. With making some approximations, the following equation can be written by using Figure 2.4.

$$ds = \frac{dx}{cos\theta} \tag{2.4}$$

Since $cos\theta \cong 1$ when $\theta$ is small, Equation 2.4 reduces to the following expression

$$ds \cong dx \tag{2.5}$$

Therefore, Equation 2.1 becomes

$$\kappa = \frac{1}{r} = \frac{d\theta}{dx} \tag{2.6}$$

Also, since $\tan\theta \cong \theta$ when $\theta$ is a small quantity. Equation 2.2 can be approximated as

$$\theta \cong \tan\theta = \frac{d\nu}{dx} \tag{2.7}$$

Thus, for small rotations of a beam, the angle of rotation and the slope are equal. Taking the derivative with respect to $x$, the following expression can be obtained

$$\frac{d\theta}{dx} = \tan\theta = \frac{d^2\nu}{dx^2} \tag{2.8}$$

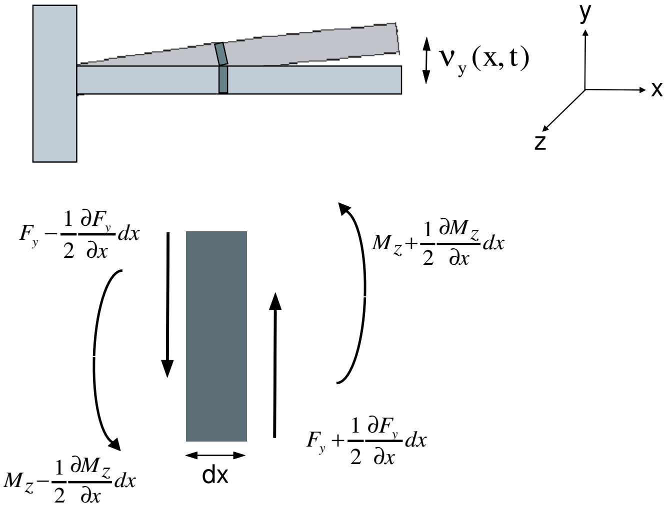

Figure 2.5: The flexural behavior of a straight cantilever beam

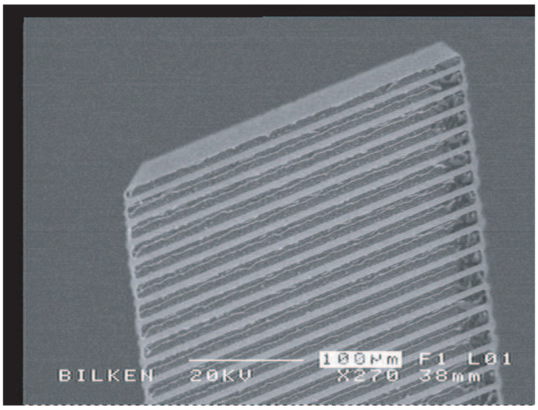

Figure 2.6: The fabricated silicon nitride bridges.

Now combining this equation with Equation 2.6, the following equation is obtained

$$\kappa = \frac{1}{r} = \frac{d\theta}{dx} = \tan\theta = \frac{d^2\nu}{dx^2} \tag{2.9}$$

This equation relates the curvature to the beam deflection $\nu$ of the beam. It is valid for a beam of any material, provided the rotations are small.

The bending moment is the resultant of stresses distributed over the cross section. With no external momentum is applied the total bending moment is equal to the moment due to the internal forces.

$$M_z = \int_A y\sigma_x = k\int_A y^2 dA \tag{2.10}$$

where $\sigma_x$ is the only remaining normal stress written as

$$\sigma_x = ky \tag{2.11}$$

also $k$ is a constant and $y$=0 lies in the center of the beam. The total internal force has to be zero and is given by

$$F_{int} = \int_A \sigma_x dA \tag{2.12}$$

where $A$ is the crossectional area.

The moment of inertia of a plane area in $z$ direction is defined as, with respect to the Figure 2.5

$$I_z = \int_A y^2 dA \tag{2.13}$$

By using Equations 2.10 and 2.13, $k$ can be defined as

$$k = \frac{M_z}{I_z} \tag{2.14}$$

Then the normal stress in the beam are related to the bending moment by substituting Equation 2.14 into the expression for $\sigma_x$, yielding

$$\sigma_x = \frac{M_z y}{I_z} \tag{2.15}$$

For the material that is elastic with a linear stress-strain diagram, Hooke's Law for unixaxial beam can be used as

$$\varepsilon_x = \frac{\sigma_x}{E} \tag{2.16}$$

and then

$$\varepsilon_x = \frac{M_z y}{EI_z} \tag{2.17}$$

Also from Figure 2.4, strain can be written as [15]

$$\varepsilon = \frac{dL - dL_o}{dL_o} = \frac{(r-y)d\theta - rd\theta}{r \sin d\theta} = -\frac{y}{r} = -\kappa r \tag{2.18}$$

This equation shows that the longitudinal strains in the beam are proportional to the curvature and that they vary linearly with the distance $y$.

Combining Equations 2.9, 2.17, and 2.18 yields the equation

$$M_z = -EI_z \frac{\partial^2 \nu(x,t)}{\partial x^2} \tag{2.19}$$

where $E$ is the elastic modulus of the beam, and $I$ is the moment of inertia. This derivation implies that the beam equation in this form only holds for beams for which all points have small slope angles.

The equation of motion for the beam, if no external force or bending moments acting on it, can be given as

$$m \frac{\partial^2 \nu(x,t)}{\partial t^2} = \sum F_{int} \tag{2.20}$$

and the total momentum must be zero

$$\sum M = 0 \tag{2.21}$$

The total force can be calculated from Figure 2.5

$$\sum F_{int} = \left(F_y + \frac{1}{2}\frac{\partial F_y}{\partial x}dx\right) - \left(F_y - \frac{1}{2}\frac{\partial F_y}{\partial x}dx\right) = \frac{\partial F_y}{\partial x}dx \tag{2.22}$$

the relationship between the bending moment and the force can be deduced from Figure 2.5 by sum of the bending moment as

$$\begin{aligned} \sum M_{int} &= \left(M_z + \frac{1}{2}\frac{\partial M_z}{\partial x}dx\right) - \left(M_z - \frac{1}{2}\frac{\partial M_z}{\partial x}dx\right) \\ &+ \left(F_y + \frac{1}{2}\frac{\partial F_y}{\partial x}dx\right)\left(\frac{dx}{2}\right) - \left(F_y - \frac{1}{2}\frac{\partial F_y}{\partial x}dx\right)\left(-\frac{dx}{2}\right) \end{aligned} \tag{2.23}$$

then

$$F_y = -\frac{\partial M_z}{\partial x} \tag{2.24}$$

By combining Equations 2.19, 2.20, 2.22 and 2.23 with the mass $m = \rho A dx$, where $\rho$ is the density of material, and $A$ is the cross-sectional area of the beam ($A$=$wt$), the equation of motion becomes

$$\rho A \frac{d^2 \nu(x,t)}{dt^2} + EI \frac{\partial^4 \nu(x,t)}{\partial x^4} = 0 \tag{2.25}$$

this is the equation for the vibration.

This equation is best solved by separation of variables [14, 16]. Note that this equation assumes that flexural rigidity, *EI*, does not change with respect to $x$. I am not concern about the complete solution of the equation, but only natural resonance frequencies of the beam. A simple way to find the natural resonance frequency, a Fourier Transformation can be applied to Equation 2.16 with $\Phi(\nu(x,t) = V(x,\omega)$ results to

$$\rho A(i\omega)^2 V(x,\omega) + EI\frac{\partial^4 V(x,\omega)}{\partial x^4} = 0 \tag{2.26}$$

this equation is rewritten to obtain a simpler form

$$-\alpha^4\omega^2 V(x,\omega) + \frac{\partial^4 V(x,\omega)}{\partial x^4} = 0 \tag{2.27}$$

where

$$\alpha^4 = \frac{\rho A}{EI} \tag{2.28}$$

The solution of this differential equation is

$$V(x,w) = C_1\sin(\alpha x\sqrt{\omega}) + C_2\cos(\alpha x\sqrt{\omega}) + C_3\sinh(\alpha x\sqrt{\omega}) + C_4\cosh(\alpha x\sqrt{\omega}) \tag{2.29}$$

$C_1, C_2, C_3$, and $C_4$ are the real constants and can be found by applying the following boundary conditions for the cantilever problem.

$$V(0,\omega) = 0 \tag{2.30}$$

$$\frac{\partial V(0,\omega)}{\partial x} = 0 \tag{2.31}$$

$$\frac{\partial^2 V(L,\omega)}{\partial x^2} = 0 \tag{2.32}$$

$$\frac{\partial^3 V(L,\omega)}{\partial x^3} = 0 \tag{2.33}$$

The boundary conditions come from the supports of a beam. The first and second conditions arise from that at the clamped side of the cantilever ($x$=*0*) there is no displacement and the beam is straight. Since at the free end of the beam ($x$=$L$), there is no bending moment and the shear force acting on the beam, these result to the last two boundary conditions.

By using the first two boundary conditions, $C_2 = -C_4$ and $C_1 = -C_3$ are found. By using the last two boundary conditions, Equation 2.20 reduces to

$$\left(\frac{1+\cos(\alpha L\sqrt{\omega})\cosh(\alpha L\sqrt{\omega})}{\sin(\alpha L\sqrt{\omega})-\sinh(\alpha L\sqrt{\omega})}\right)=0 \tag{2.34}$$

A nontrivial solution can be found if

$$\cos(\alpha L\sqrt{\omega})\cosh(\alpha L\sqrt{\omega})=-1 \tag{2.35}$$

This equation can be solved numerically by using the following substitution

$$k=\alpha L\sqrt{\omega} \tag{2.36}$$

The roots of Equation 2.27 give the modes of vibration for the cantilevers, $k_n$'s. The equation gives the natural frequencies of the beams as

$$\omega_n=\frac{k_n^2}{L^2}\sqrt{\frac{EI}{\rho A}} \tag{2.37}$$

The fundamental frequency for the cantilever beam as

$$f_o=0.1615\left(\frac{t}{L^2}\right)\sqrt{\frac{E}{\rho}} \tag{2.38}$$

here the bending moment of inertia for a rectangular beam is given by $\frac{1}{12}wt^3$ [15].

The fundamental resonance frequency for a beam clamped at both ends

$$f_o=1.03\left(\frac{t}{L^2}\right)\sqrt{\frac{E}{\rho}} \tag{2.39}$$

can be found by using the following boundary conditions

$$V(0,\omega)=0 \tag{2.40}$$

$$\frac{dV(0,\omega)}{dx}=0 \tag{2.41}$$

$$V(L,\omega)=0 \tag{2.42}$$

$$\frac{dV(L,\omega)}{dx}=0 \tag{2.43}$$

The resonance frequency is proportional to the square root of Young's modulus and to the beam thickness, and inversely proportional to the square of the length and the square root of density. This shows that reducing the size or magnitude of some parameter while other parameters are constant, the decrease or increase in resonance frequency can be obtained. Therefore, cantilever sensors with extremely high sensitivity, high energy efficiency, and faster time response can be fabricated by simply reducing the cantilever dimensions. However, reducing the dimensions can cause difficulties in fabrication as well as monitoring the beam response.

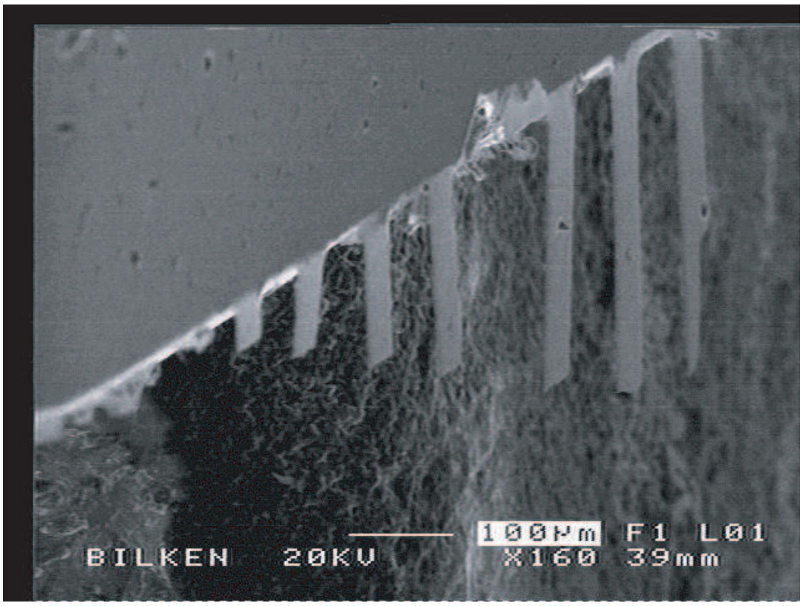

Figure 2.7: The fabricated silicon nitride cantilevers

## 2.2 The Quality factor of a beam

The frequency response of a resonator is generally characterized by its resonance frequency and the quality factor. The Q-factor of a beam, defined as the total energy stored in the structure divided by the sum of the energy losses from the vibrating elements for one cycle [10, 17].

$$Q = 2\pi \frac{\texttt{stored vibration energy}}{\texttt{dissipated energy in a period}} \tag{2.44}$$

The stored vibration energy is equal to the maximum kinetic energy and the dissipated energy per period is equal to the integration over the period of the product of the dissipative part of the drag force and the velocity with $T = \frac{2\pi}{\omega}$, being the period. The Q-factor can be calculated by determining the logarithmic decrement of the vibration in the case of weak damping or it can be measured from the amplitude-frequency spectrum of the vibration. The latter method is defined as the ratio of the resonance frequency, $f_o$, to the frequency bandwidth, $\Delta f$, at the -*3dB* amplitude points, as shown in Figure 2.8 [10].

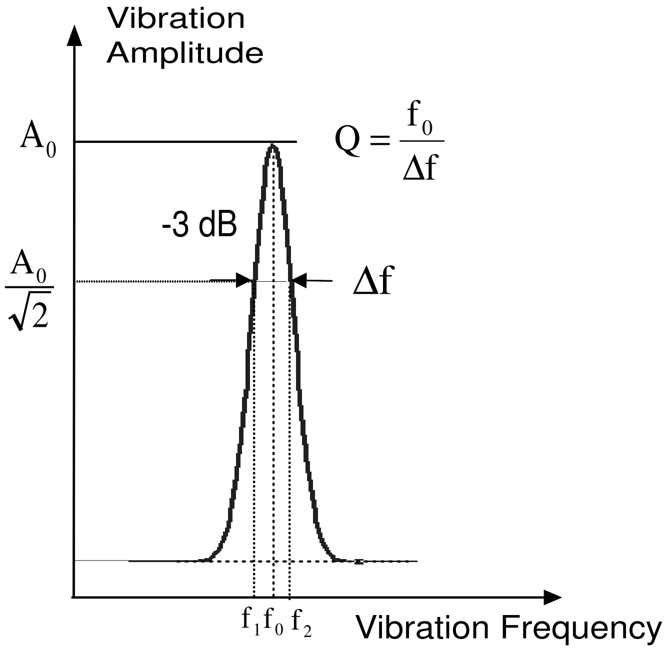

Figure 2.8: Amplitude versus Frequency curve for a cantilever

$$Q = \frac{f_o}{f_2 - f_1} = \frac{f_o}{\Delta f} \tag{2.45}$$

Bandwidth $BW$ or $\Delta f = f_2 - f_1$, where $f_2$ is the upper and $f_1$ the lower cutoff frequency. On a graph of amplitude response versus frequency, the bandwidth is defined as the 3 *dB* change in level (voltage, current or amplitude) on either side of the center frequency. The Figure 2.8 also shows that the Q-factor is high when the resonance peak in the frequency-amplitude spectrum is narrow and high that makes the micro-sensor more effective in identifying a desired signal. This method is used in our case to measure the quality factor of our resonant beams. The Q-factor is an important parameter because it reflects the resolution of the sensor. Systems with a high Q-factor resonate with a greater amplitude (at the resonant frequency) than systems with a low Q-factor for a given excitation amplitude. A high mechanical Q-factor also shows that the sensor performance mostly depends on the mechanical properties of the resonator element [10]. From the definition of the Q-factor, the higher Q values result from the reductions in dissipation losses. The quality factor of a beam can be manipulated by knowing what factors contribute to energy dissipation.

## 2.3 Loss mechanisms

Environmental conditions, such as local pressure and temperature, have more effects on the micro-mechanical devices than conventional machines. Damping decreases the quality factor. Damping can be defined as dissipation of oscillatory or vibratory energy with motion or with time. There are several dissipation losses occurring through viscous damping and acoustic damping, anchor losses for physically-fixed devices, thermoelastic damping and other sources [14]. An individual quality factor can be assigned to the different mechanisms. The overall Q-factor of a system can be found by the sum of the inverses of the individual Q-factors [10].

$$\frac{1}{Q_{tot}} = \sum \frac{1}{Q_i} \tag{2.46}$$

Instead of calculating the total damping parameters in every region, the dominant parameters in that region can be approximated.

### 2.3.1 Air-damping effect

The air-damping has been shown to be the most profound effect for the devices operated in open air or low vacuum among the sources of damping effects [18, 2]. Air-damping generally shifts the resonance frequency towards smaller values and degrades the quality factor as the dimension of the beam gets smaller. Because, the volume (mass) decreases more rapidly than the surface area of the beam [2]. The different air drag mechanisms are characterized in different regions. There are mainly three regions, the intrinsic region, the molecular region, and the viscous region, in the pressure range from vacuum to atmospheric region.

In the intrinsic region, the damping parameters and the corresponding Q-factor are independent of air pressure and the geometry of the beam because of the fact that the air pressure is so low in this region. Hence, the quality factor reaches its maximum value.

In the molecular region or Knudsen region, independent collisions of the non-interacting air molecules cause to damping. Kinetic theory of gases is used to determine the drag force in this region. The damping parameter, $\gamma_1$, related to air pressure $p$ and the width of the beam, $w$, is given by the following equation [17].

$$\gamma_1 = k_m w p \tag{2.47}$$

and

$$\gamma_2 = 0 \tag{2.48}$$

here $\gamma_1$ and $\gamma_2$ are damping parameters and

$$k_m = \left(\frac{32M}{9\pi RT}\right)^{\frac{1}{2}} \tag{2.49}$$

where $M$ is the mass of the gas molecules ($M_{air}$=28.964 $g/mole$), $R$ is the gas constant , and $T$ is the absolute temperature. At room temperature $T$ (=*300 K*), $R$ (*8.314472* $J.K^{-1}mole^{-1}$) and $k_m$=$3.6 \times 10^{-3}$ $s/m$. The Q-factor can then be written as [17]:

$$Q = \frac{\rho A f}{\gamma_1} = \left(\frac{9\pi RT}{32M}\right)^{\frac{1}{2}} \frac{t\rho f}{p} \tag{2.50}$$

here $f$ is the damped angular frequency [17].

The third region, viscous region leads up to the atmospheric pressure. This region is mainly discussed in this study. In this region, air acts as a viscous fluid and the drag force can be determined by using the fluid mechanics. The air is assumed as incompressible and Reynolds number is small, because the velocity of the vibrating beam is always much smaller than the speed of sound [17]. Since it is difficult to determine the velocity field of the air around the vibrating beam, the beam will be approximated as a string of spheres which are vibrating independently of each other. Then the resulting drag force is equal to the sum of the drag forces of the individual spheres. The Navier-Stokes equation and the continuity equation can be applied for the velocity field u(x,y,z,t) as [17]:

$$\frac{\partial \mathbf{u}}{\partial t} + (\mathbf{u}.\nabla)\mathbf{u} = -\frac{1}{\rho_o}\nabla p + \frac{\mu}{\rho_o}\Delta \mathbf{u} \tag{2.51}$$

$$\nabla \mathbf{u} = 0 \tag{2.52}$$

where $\mu$ is the dynamic viscosity and $\rho_o$ is the density of the medium. For ideal gases:

$$\rho_o = \frac{M}{RT} p \tag{2.53}$$

Then for small Reynolds numbers, the drag force for an oscillatory motion on the surface with radius $R$ can be calculated by using Equations (2.50) and (2.51) [17].

$$F_{drag} = (\beta_1 + j\beta_2)v = \beta_1 v - \frac{\beta_2}{f} v = \gamma_1 L v - \frac{\gamma_2 L}{f} v \tag{2.54}$$

where $v$ is the velocity of the vibrating beam in the complex form as $v = v_o e^{-jwt}$ to obtain a complex drag force, and $L$ is the length of the beam. $\gamma_1$ and $\gamma_2$ are proportional to the quality factor and the frequency shift, respectively. The parameters $\beta_1$ and $\beta_2$ here is given by [17]:

$$\beta_1 = 6\pi\mu R \left(1 + \frac{R}{\delta}\right) \tag{2.55}$$

and

$$\beta_2 = \frac{2}{3}\pi R^3 \rho_o \left(1 + \frac{9}{2}\frac{\delta}{R}\right) f \tag{2.56}$$

then the drag force is given by the equation:

$$F_{drag} = \left[6\pi\mu R \left(1 + \frac{R}{\delta}\right) + j\frac{2}{3}\pi R^3 \rho_o \left(1 + \frac{9}{2}\frac{\delta}{R}\right) f\right] v \tag{2.57}$$

here $j$ is the complex number, $f$ is the resonance frequency and $\delta$ is the region around the beam where the motion of the gas is turbulent. The width $\delta$ depends on the pressure and is given by [17]:

$$\delta = \left(\frac{2\mu}{\rho_o f}\right)^{\frac{1}{2}} \tag{2.58}$$

The Q-factor of a vibrating beam in the viscous region, approximated by an oscillating sphere, is given by the equation [17]:

$$Q = \frac{\rho A f_o}{\gamma_1} = \frac{\rho A L}{6\pi\mu R}\left(1 + \frac{R}{\delta}\right)^{-1} f_o \tag{2.59}$$

where $\varrho$ is the density of the beam.

#### 2.3.1.1 Squeeze Force damping effect

If the gap between the beam and the supporting surface is small, a squeeze force acts between the beam and the surface. This damping can be thought of as energy being transferred from the motion of the beam to the movement of air molecules. Squeeze force damping results when a pressure difference occurs between the gap and the environment. The pressure assumed to be constant around the resonator might not be true because of the fact that when the device moves close to the surface or moves away from the surface, the air film in the gap is squeezed. This movement introduces an inhomogeneous pressure distribution underneath the resonator. The speed of the movement of the device is reduced in this gap. Therefore, the pressure underneath the resonator is higher than that above the resonator [19]. As the gap size decreases, the damping force increases. For that matter, micromechanical vibrating structures, also nanomechanical ones, are needed to be operated under vacuum.

### 2.3.2 Surface-related effects

To achieve adequate conductivity of the resonator, a thin metal film layer can be deposited on the resonator. This metal layer decreases the quality factor of the resonator linearly as the thickness of the metal layer increases [20]. In our study, some of the beams, such as the bridges and $Si_3N_4$ cantilevers, are covered with a 50 nm thick Aluminum metal layer to provide a reasonable reflection for optical detection. However, metal layer related effect has a significant contribution mainly on nanometer scale devices. The effects may be due to the difference in restoring forces between the metal and a silicon nitride layers or the higher internal friction of the metal with respect to the silicon nitride.

When the device is exposed to air, a thin amorphous native oxide layer grows on the device or contaminant molecules attach to the surface of the layer. This also creates an additional stress at the interface. Removing this monolayer native oxide by some techniques, such as heat treatment, can increase the quality factor significantly [21]. Beside the native oxide layer, a water layer found in the atmosphere also increases the loss especially in silicon NEMS resonators. Because, water increases the internal friction of $SiO_2$ by forming vibrating Si-OH groups [22].

### 2.3.3 Clamping-Anchor losses

Anchor points can be defined as the locations where the beam is suspended by the material which is in contact with the substrate. The anchor points of the beam studied in this thesis are the end of the beams. Anchor points and substrate below reduce the vibration energy of the beam in such a way that, at the contact area of the beam and the clamp, slipping occurs while the beam bends. This microslips and local deformations result in the energy dissipation from the resonator via the clamps. The loss energy is related to the stiffness of the beam. When the stiffness increases, the vibrational energy lost increases. This damping mechanism mainly occurs in micro-scale resonators. Anchor loss can be reduced by two methods which isolate the resonant structure from the substrate. The first one is the double beam in parallel, such as a tuning fork, resonating 180° out of phase with respect to one another [23]. The second one is the free-free beam that is a suspended location which does not move during the oscillation [24].

### 2.3.4 Internal losses

The internal losses are another factor which reduces the quality factor of the resonators. It depends on the material properties such as purity, dislocations, and thermoelastic losses of the material. The thermoelastic loss has relative importance with the size of the structure, for nanoscale structures it is less important than another intrinsic mechanisms such as intrinsic phonon-phonon scattering [25]. Thermoelastic dissipation is known to be a significant loss mechanism near room temperature for the case a beam in flexure [26]. Thermoelastic dissipation arises from thermal currents generated by pressed or rarefied regions. Also the quality factor reducing contribution from the material to the net quality factor can be neglected for the single-crystalline material, such as silicon or quartz, because, there are no losses in a perfect crystal. Then single-crystalline material has a higher Q than a polycystalline material [10].

# Chapter 3

# DEVICE FABRICATION

This chapter is devoted to the design and fabrication of microdevices. The methods used in fabrication process are explained in detail. The material used for device fabrication are silicon nitride ($\mathtt{Si_xN_y}$) and SOI (Silicon on Insulator). Silicon nitride is a man made compound. It is light, hard, and has low thermal expansion coefficient. It has high mechanical strength, fracture toughness, and it is resistant to deformation at room temperature as well as at elevated temperatures. Its Young's modulus is higher than that of silicon and its intrinsic stresses can be controlled by the specifics of the deposition process. It is an effective masking material in many alkaline etch solutions [27]. Utilization of silicon on insulator has a higher performing, lower power (dynamic) devices than traditional bulk silicon techniques. For silicon cantilevers, SOI platform which has a silicon device layer with 4 $\mu m$ thick on an oxide layer. The thickness of the double sided-polished SOI wafer is 400 $\mu m$. For silicon nitride bridges and cantilevers, both side nitride coated and polished silicon wafer is used. The thickness of the coated nitride is 2 $\mu m$ for cantilever and 0.5 $\mu m$. The thickness of the silicon wafer is 400 $\mu m$. The resonators studied in this thesis have the following fabrication process steps: Cleaning, Photolithograhy, Wet Etching (etching with KOH and HF, Reactive Ion Etching of SOI cantilevers), PECVD nitride deposition, Aluminium metal coating.

## 3.1 Cleaning

Cleaning is the first step of the fabrication. Some typical contaminants must be removed chemically prior to the photoresist coating. These contaminants are dust from scribing or cleaving, atmospheric dust, photoresist residue from the previous photolithography, lint from wipers, oil, $H_2O$ residue, developer residue etc. These factors can be minimized by, for instance, using laser scribing, good clean room practice, good DI water system and using lint-free wipes in addition to the cleaning process. The samples are cleaned orderly by using Aceton, Isopropanol, and $H_2O$, and dried by nitrogen.

## 3.2 Photolithography

Photolithography can be defined as the process of the transferring of the patterns on a mask onto the surface of a wafer or a chip. Photolithographic process involves the following steps: photoresist coating, soft baking, mask alignment, exposure, development and hard baking.

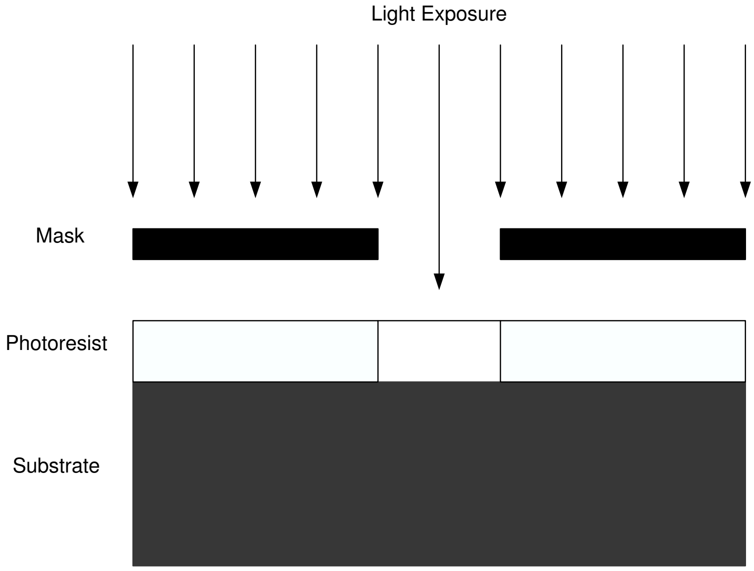

Figure 3.1: Photolithography process

Photoresist coating step can be explained as covering the surface of the substrate with a polymer based photoresist that changes its properties under the exposure of certain wavelengths (usually UV light) of the light. The resist firstly is dropped to the surface of the substrate by using a drop wise and then the sample with resist on is spun on a resist spinner. Spinning speed is set to 4000-6000 rpm, depending on the required resist thickness. As the rotation speed increases, the resist layer becomes thinner. Spin time is also an important factor in determining the resist thickness, and it is usually set to 40 s in this work. AZ 5214 photoresist is used in the fabrication of the devices.

There are two types of photoresist: positive resist and negative resist. With the positive resist, the part which is exposed to the UV light can be removed in a solution called developer. Because the UV light changes the chemical structure of the resist, it becomes more soluble in the developer. Negative resist behave in the opposite manner. The UV light causes the negative resist to become polymerized and more difficult to solve. Then the unexposed part become soluble in the developer. Therefore the inverse of the pattern on the mask is transferred to the substrate. Figure 3.2 shows the pattern differences generated by the positive and the negative resist.

Soft-baking step has a very critical effect in photo-imaging. All of the solvents are removed from the photoresist coating during the soft baking process. The photoresist become photosensitive after the soft-baking. Hard-baking causes to decrease the photosensitivity of resist in two ways. First is to reduce the solubility of the developer. The other way is to destroy a part of the sensitizer. Undersoft-baking also causes to prevent the light from reaching the sensitizer. In our fabrication process, the hot plate is adjusted to 110 $^{\mathbf{o}}\mathbf{C}$ - 120 $^{\mathbf{o}}\mathbf{C}$ for 50-55 seconds for soft-baking process.

Mask alignment is one of the important step in photolithography process. A mask which is glass or quartz plate with a patterned metal film (usually Chromium) on one side is placed on the sample. The sample with photoresist is exposed to the UV light then the pattern on the mask is transferred to the surface of the sample. The resist-coated wafer is either in contact with the mask

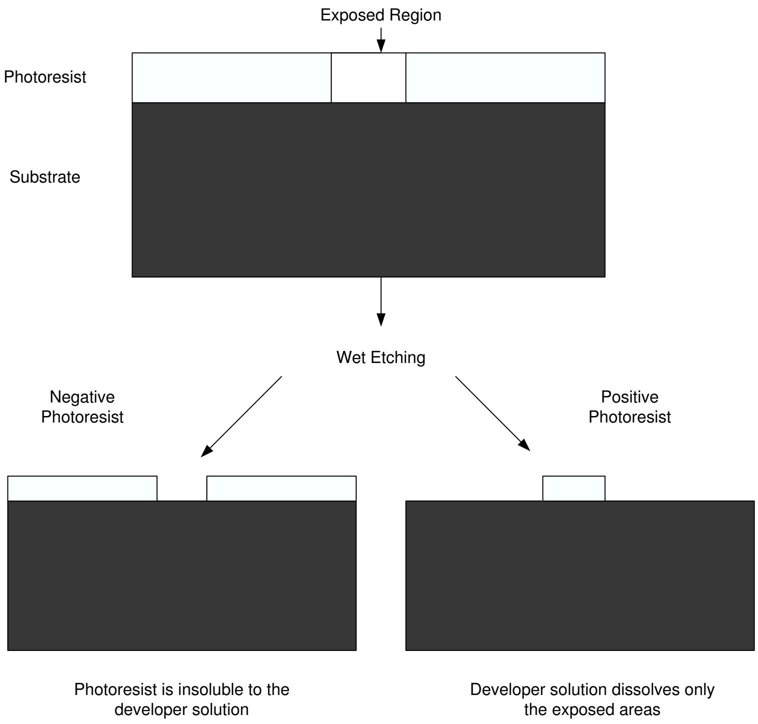

Figure 3.2: Comparison of negative and positive resists

to get very high resolution or held at a small gap to eliminate the mask damage. Contact printing damages the mask and causes defects in the pattern.

The next step for the photolithographic process is the development. A developer removes either the exposed or unexposed resist layer depending on the solubility of the resist. The solubility of the resist can vary with some parameters. These are initial resist thickness, prebake conditions, developer chemistry, and developing time. AZ 400 developer is used in the fabrication of resonators. It is mixed 1:4 ratio with water (AZ 400 : $H_2O$). The development time changes between 20 to 30 seconds in our fabrication process.

Hard-baking is the final step in the photolithographic process. This step is used to harden the photoresist and improve adhesion of the photoresist to the wafer surface before the etching process. The samples in this study is left 5 minutes on the 120°C hot plate before the HF etching process.

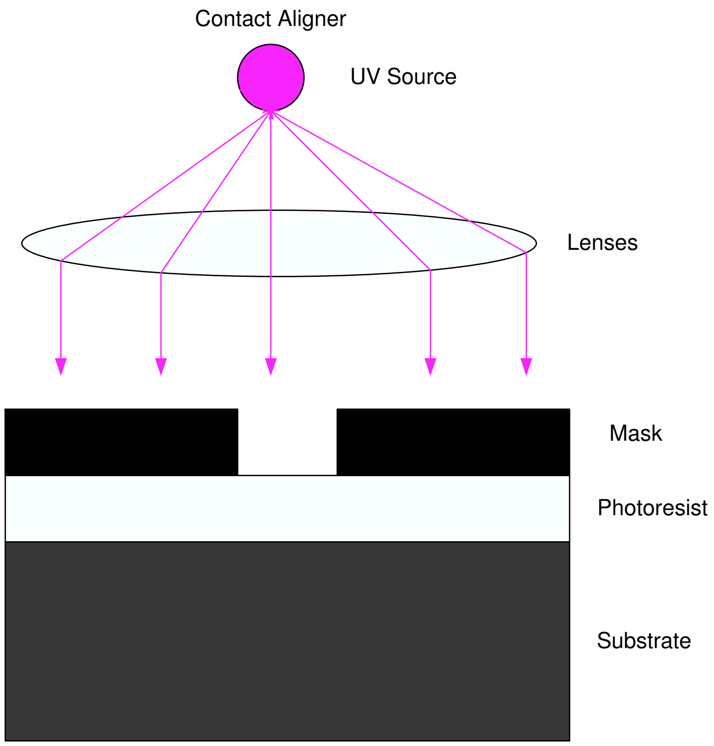

Figure 3.3: The exposure method: Contact mode

## 3.3 Etching

Etching can be defined as removing some part of the wafer, either from the silicon substrate itself or from any film or a layer of material on the wafer. There are two types of etching: wet etching and dry etching.

In wet etching the material is dissolved from the surface when immersed in a chemical solution. This is a simple technology if the suitable combination of etchant and the mask material is found for the application. Etchant removes materials from the wafer, usually in specific patterns defined by photoresist masks on the wafer. Materials not covered by these masks are 'etched away' by the chemicals while those covered by the masks are left almost intact. These masks can be deposited on the wafer in an earlier step such as lithography or deposition. Wet etching fall into two categories: isotropic and anisotropic wet etching.

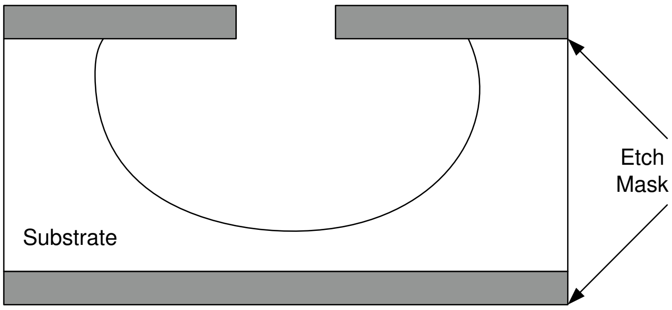

Figure 3.4: Isotropic Wet Etching, the undercutting problem

Isotropic etchants attack the material in all directions at the same rate. Then they remove material horizontally under the etch mask (undercutting) at the same rate as they etch through the material. Undercutting is a big drawback of isotropic etchants. HF (hydroflouric acid) is identified an example for isotropic wet etching. This undercutting problem is illustrated for a thin film of nitride on a silicon wafer in Figure 3.4. Etchant etches the silicon faster than the nitride film. This problem is seen in the fabrication of our devices as in Figure 3.5. We overcame the undercutting problem by using the less concentration of HF in water (e.g., 1:100, HF:$H_2O$). In the fabrication of silicon nitride cantilevers and bridges, the patterned nitride film is etched by using HF with the ratio of less then 1:100.

Anisotropic etching in contrast to isotropic etching means different etch rates in different crystallographic directions in the material. The most popular anisotropic etchant which is also used in the fabrication of our devices is KOH (potassium hydroxide solution with 20 %), since it is the safest to use. The simplest structures that can be formed using KOH to etch a silicon wafer with the most common crystal orientation (100) are shown in Figure 3.6. The undercutting problem is also encountered in KOH etch process. The result is a pyramid shaped hole instead of a hole with rounded sidewalls obtained with an isotropic etchant. KOH etches slowly both oxide and nitride. Then oxide and nitride can be used as an etch mask. Oxide is suitable for short periods in the KOH etch bath. For long periods nitride is more suitable etch mask, because it etches more

Figure 3.5: The undercutting problem in the fabrication of beam process

slowly than oxide in KOH solution. Anisotropic etching allow the etching to stop on certain crystal planes in the substrate, but still results in a loss of space, since these planes cannot be vertical for (100) surface to the surface when etching holes or cavities. The cantilevers and bridges shown in the Figure 3.7, have been etched by using KOH with the ratio of 1:4, ($KOH : H_2O$). Some isopropanol alcohol is added to this solution to get higher uniformity. Its temperature is adjusted to 60°C and its spirrer is also adjusted to 300-400 rpm. KOH could etch at a rate of 16-20 $\mu m/hr$ with this recipe.

Dry etching can be defined as removing the desired part of the material by exposing this part to the bombardment of ions. The most common type of dry etching for micromachining applications is reactive ion etching (RIE). In reactive ion etching process, etchant gas is introduced into the chamber continuously and plasma is created by RF power. Then reactive species such as ions and radicals are generated in plasma for bombardment and chemical reaction respectively. The species are absorbed on the sample and then chemical reaction occurs and the products leave the surface as volatile gases. Reactive ion etching is an anisotropic etching but not depend on the crystal planes as in Wet etching. $Si$, $SiO_2$, $Si_3N_4$, $GaAs$, $Al$ can be etched with suitable gases by using the reactive ion etching

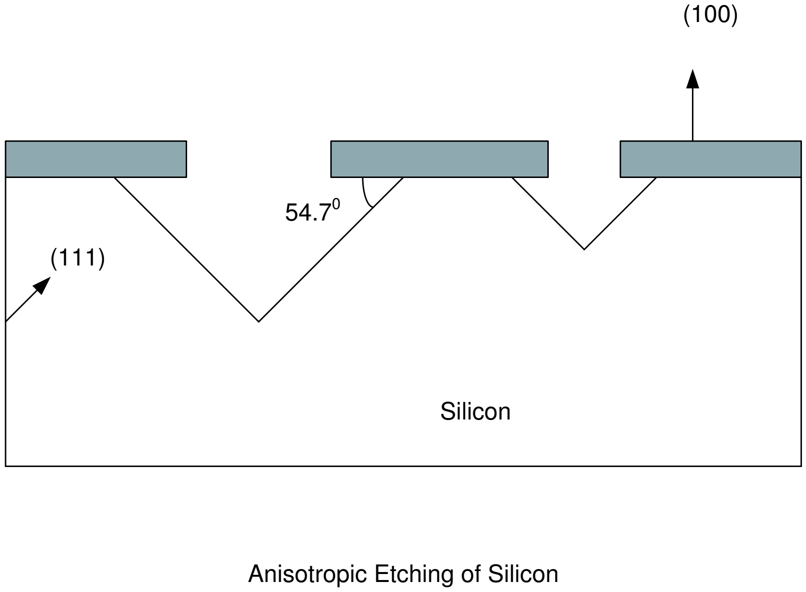

Figure 3.6: Anisotropic Wet Etching

process. The device layer of 4 $\mu m$ thick silicon in SOI wafer is etched by using RIE, (Leybold AG 301), in the fabrication of the SOI cantilevers. The problem about this technology is that it is expensive compared to wet etching. But, if the feature resolution in thin film structures is important or the vertical sidewalls for deep etchings in the substrate are necessary, dry etching is preferred.

## 3.4 Deposition

One of the basic processing steps is the deposition of thin films of material. Chemical vapor deposition working principle relies on a chemical reaction which occurs in vacuum at high temperatures. Then the reacted species deposited on the heated substrate. Common thin films deposited by using this technique are polysilicon, silicon oxides, silicon nitrides, etc. One of the chemical vapor deposition technique is the plasma enhanced chemical vapor deposition, PECVD. The working principle of this technique is that one or more gaseous species in the reactor are used to form a solid insulating or conducting layer on the surface of a wafer, with the enhancement of the process by the use of a vapor containing

Table 3.1: The growth of nitride film by using PECVD technique

| Parameter | Value | Units |
|---|---|---|
| $SiH_4$ | 180 | Sccm |
| $NH_3$ | 45 | Sccm |
| Process Pressure | 1.0 | Torr |
| Substrate Temperature | 250 | $^oC$ |
| Refractive Index | 1.74 | N/Å |
| Etch Rate | 120 | Å/min |

electrically charged particles or plasma, at lower temperatures. Since the plasma in the reactor also supplies extra energy to the gas molecules. Silicon nitride is obtained by reacting the silane ($SiH_4$) with ammonia ($NH_3$) in a plasma enhanced deposition chamber in our process. Hydrogen is a byproduct of this reaction. The refractive index of the film gives information about the impurity content and the overall quality of silicon nitride thin film. The refractive index of the film with PECVD technique is generally in the range between 1.8 and 2.5 [27]. However in our process, the refractive index of the deposited silicon nitride film is 1.74 . The most important advantage of PECVD nitride is the controlling of the film stress during deposition. Nearly unstressed films can be obtained if the deposition parameters are adjusted right. The following recipe in the Table 3.1 is used in the deposition of the silicon wafer.

## 3.5 Metallization

Metallization process can be defined as a layer of metal deposited on the wafer surface to provide electrical contacts to the devices. In this study, Aluminum metal is deposited on to the silicon nitride bridges and cantilevers that is also used for reflecting the light coming from the light source. The box-coater (Leybold, LE 560) is used for metal deposition. The working principle of the box-coater is that the material, Al (in our case), is evaporated thermally in high vacuum then this vaporized metal is deposited onto the sample surface. 50 nm Al was deposited on the wafer for the fabrication of silicon nitride bridges and cantilevers. The pressure in the vacuum chamber is about $10^{-6}$ mbar during the evaporation process. But the Al deposition onto the surface of the silicon nitride cantilever produces stress that causes the bending of the cantilevers. This problem especially effects the measurements made in testing techniques for finding the resonance frequency of the cantilevers.

The fabricated bridges and cantilevers are shown in Figure 3.8 and 3.9 respectively.

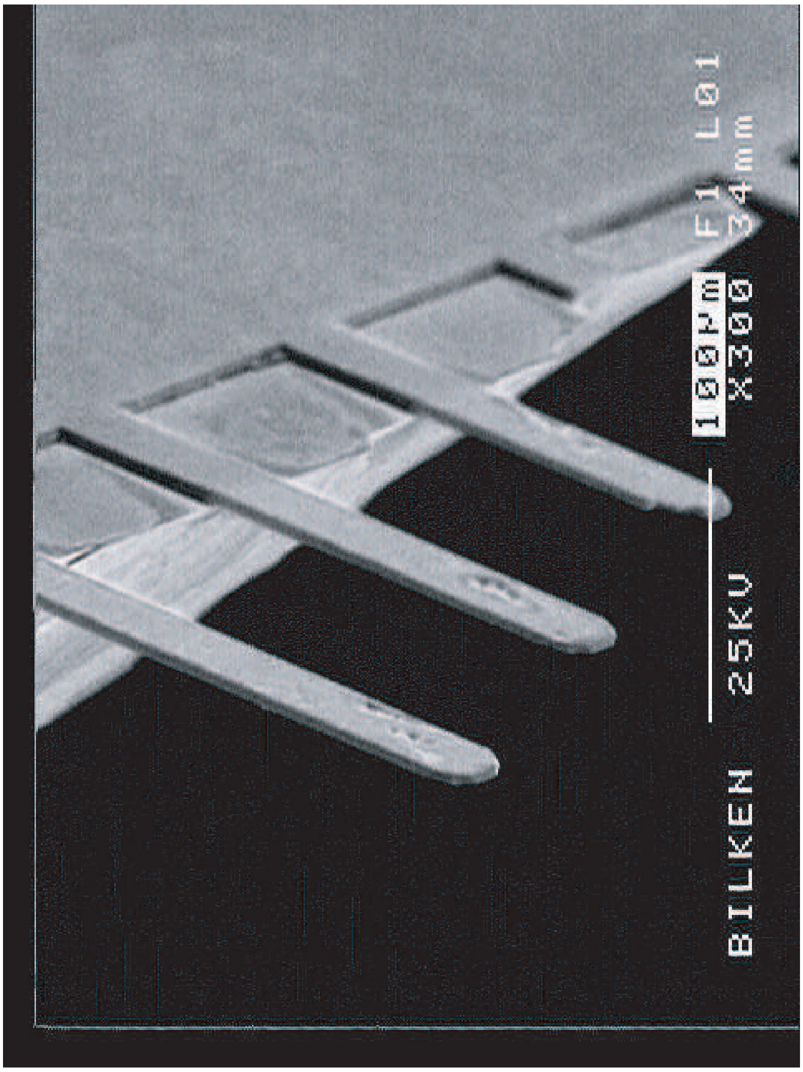

Figure 3.7: Cantilevers etched by using the KOH solution from the back side of the SOI cantilevers

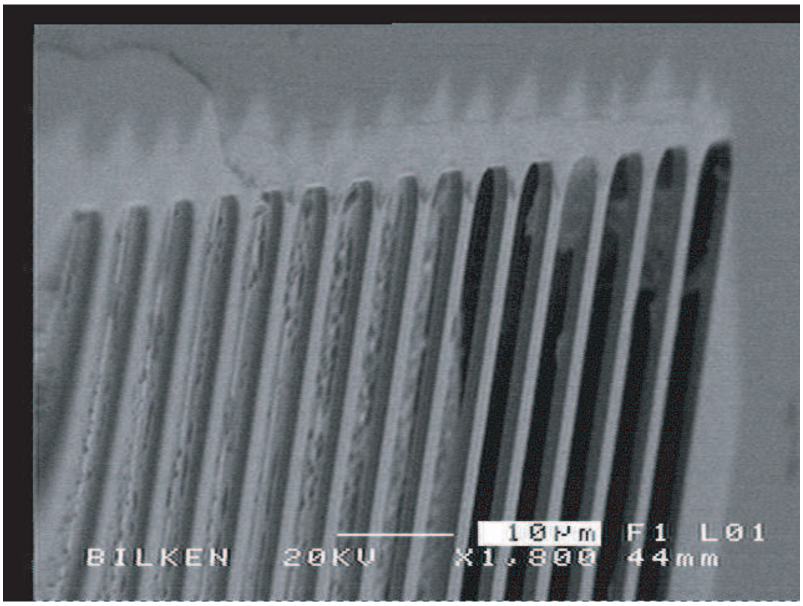

Figure 3.8: The fabricated silicon nitride bridges

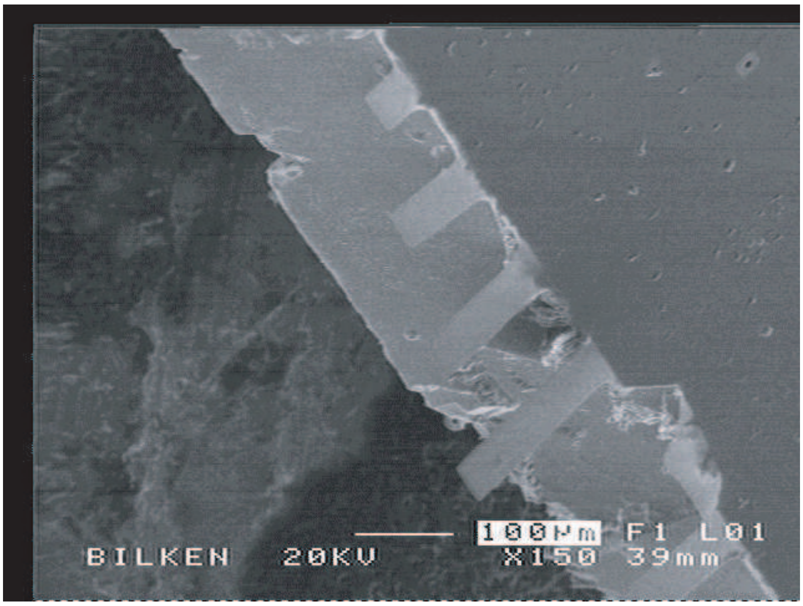

Figure 3.9: The fabricated silicon nitride cantilevers

# Chapter 4

# BEAM CHARACTERIZATION AND ANALYSIS

The characterization of the cantilever and bridge beams are performed by using two techniques. The first method is based on electrostatical actuation of the cantilevers and bridges and detecting the deflection by using a fiber optic interferometer. The second method relies on the beam deflection method using an Atomic Force Microscope head.

## 4.1 Fiber Optic Interferometer Technique

The set-up utilizing first fiber optic interferometer also includes a laser diode, a high voltage generator, a signal generator, a lock-in amplifier and a cantilever holder as shown in Figure 4.1

Al coated cantilever and bridges are attached to the cantilever holder as shown in Figure 4.1. This holder is designed to be capable of moving in three dimensions, $x$, $y$, and $z$. A piezoelectric element is glued on this translation system. The beams are placed on the piezoelectric material. The cantilevers and bridges are excited by electrostatic forces. In this excitation scheme, a conductive wire is placed near

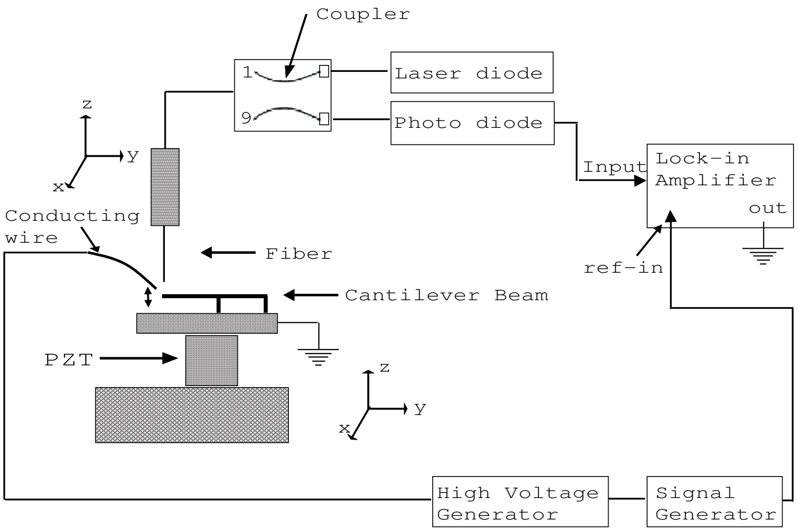

Figure 4.1: The connection scheme and the block diagram of the Fiber Optic Interferometric Technique

to the cantilevers and bridges. They are grounded by using a silver paint and a piece of wire. The conductive wire is connected to a high voltage power supply and a signal generator. The electrostatic force between the cantilever and the conductive plate is given by [28]

$$F = \frac{V^2}{2}\frac{\partial C_{(z)}}{\partial z} \tag{4.1}$$

where $z$ is the distance between the cantilever and the wire. The given excitation voltage has the form as

$$V_t = V_{DC} + V_{AC}\cos(\omega t) \tag{4.2}$$

The resulting electrostatic force has $AC$ and $DC$ components and has the form

$$F \cong \frac{1}{2}\frac{\partial C_{(z)}}{\partial z}[V_{DC}^2 + 2V_{DC}V_{AC}\cos(\omega t)] \tag{4.3}$$

$DC$ bias is given much larger than $AC$ amplitude ($V_{DC} \gg V_{AC}$), then the second harmonic of the AC term can be neglected. The excitation of the cantilevers and bridges $V_{DC}$ is adjusted to 50 V and $V_{AC}$ is adjusted to 1 V. In this excitation scheme, cantilevers and bridges response is measured over a broad frequency range. The frequency ranges adjusted by using Lock-in Amplifier.

A fiber-optical interferometer is used for deflection detection in the system. Typical sensitivity of such an interferometer is generally around $10^{-3}/Hz^{1/2}$ with few $\mu W$ of optical power incident on the cantilever and such low powers are also desired to reduce the back-action of laser light on the cantilever [28]. The laser diode current is adjusted to 8 mA and the corresponding optical power is measured as $P_{LD}$=1.5 mW. The optical coupler has a coupling ratio of $\alpha_c$ (using a 10 % -90 % coupler). The power coupled to the cavity arm of the coupler, $P_i = \alpha_c P_{LD}$, is 150 $\mu W$.

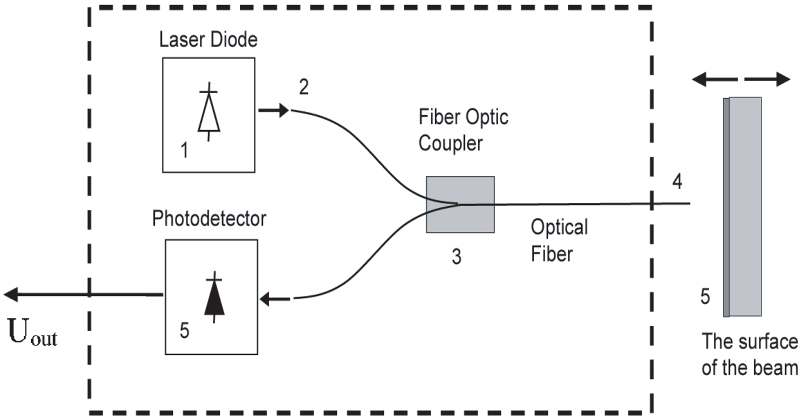

Figure 4.2: The operation principle of the fiber optic interferometer

A fiber-optic interferometer consists of a laser source (Spectra Diode Labs, SDL 800, Laser Diode Driver with a wave length of $\lambda = 1310\ nm$), a fiber optic coupler, and photodiodes for monitoring the laser power and the interference signal. In this system the gap between the end face of the fiber and the surface of the cantilever beam act as a cavity. Optical interference occurs in this micron-sized cavity formed between the end face of the optical fiber and the surface of the beam (acting as a mirror). Figure 4.2 shows the operation principle of the fiber optic interferometer. The radiation of the laser diode 1 is coupled into the fiber 2 and propagates through the coupler 3 to the fiber end face 4. Then some part of the radiation is reflected back from the end face of the fiber and the other of the radiation is transmitted to air, reflected from the surface of the beam and return to the fiber 4. Then the optical beam reflected from the end face of the fiber interferes with the beam reflected of the surface of the cantilever or bridge. The interferometer response can be modelled as a simple two-component interference.

The current from the signal photodiode is given by [29]

$$i = i_o \left[1 - V \cos\left(\frac{4\pi d}{\lambda}\right)\right] \tag{4.4}$$

where $\lambda$ is the current laser wavelength and d is the fiber-to-cantilever distance. The quantities $V$ and $i_o$ correspond to the fringe visibility and the average current, respectively, and are given by

$$V = \left(\frac{i_{max} - i_{min}}{i_{max} + i_{min}}\right) \tag{4.5}$$

and

$$i_o = \left(\frac{i_{max} + i_{min}}{2}\right) \tag{4.6}$$

where $i_{max}$ and $i_{min}$ are the currents corresponding to maximum constructive and destructive interference, respectively. The average current and visibility can also expressed by different parameters [30] which are as follows:

$$i_o = P_{av}S = (P_r + P_s)S \tag{4.7}$$

and

$$V = 2\sqrt{P_r P_s}(P_r + P_s) \tag{4.8}$$

where $P_r$, $P_s$, $P_{av}$, and $S$ are reference and signal power at the photodiode, average power incident on the photodetector and the photodiode sensitivity, respectively.

The cantilevers and bridges are coated with 50 nm thick Al thin film and this results in a higher back reflection. In reality, the diffraction of the light and small diameter of the fiber core ($\sim 9\mu m$) cause only a small portion of the reflected light to couple into fiber 4. An other important parameter which changes the collection of reflected light is the hardness of the alignment of the above mentioned two surfaces to be parallel. If the fiber is gold coated, then some part of the light is reflected back in to the fiber. The rest impinges on the back of the cantilever and reflected from it. Therefore we obtain multiple reflections which form a Fabry-Perot interferometer cavity between the end face of the fiber and the back of the cantilevers or bridges. This causes radical enhancement in the sensitivity. In the presence of multiple reflection photodiode current can be expressed on

$$i = i_o \left[1 - VF\left(\frac{4\pi d}{\lambda}\right)\right] \tag{4.9}$$

where $F$ is a periodic function of $d$. The multiple reflections enhances the sensitivity. The most sensitive operation is where the phases of the two reflected components are in quadrature, or d=$\frac{\lambda}{8}$, $\frac{3\lambda}{8}$, $\frac{5\lambda}{8}$,....At quadrature, changes in photocurrent, $\Delta i$ response for small changes in distance, $\Delta d$, and wavelength, $\Delta\lambda$, is given by

$$\frac{\Delta i}{i_o} = 4\pi V\frac{\Delta d}{\lambda} - 4\pi V d\frac{\Delta\lambda}{\lambda^2} \tag{4.10}$$

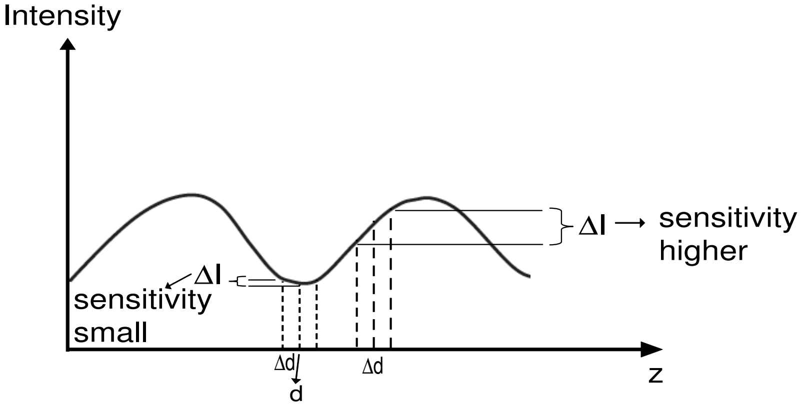

Figure 4.3: Interference signal versus cavity length

A typical interference signal versus cavity length graph is shown in Figure 4.3 to help us adjust where the intensity sensitivity is higher. This can be done with the help of the XYZ-micropositioner of the fiber or sweeping the cavity length by using a piezoelement mounted on this micropositioner and connected to a high voltage generator.

The intensity of the optical radiation at the surface of photodetector 5 is periodically changed with the distance $d$ (cavity length) between the fiber and the beams. The back reflected signal from the beams produces a phase shift that depends on the distance $d$, as follows [28]

$$\varphi = \varphi_r + \frac{4\pi d}{\lambda} \tag{4.11}$$

here $\varphi_r$ is the phase shift because of the reflection and it does not depend on the $d$.

In general, because of the divergence of the light at the output of the fiber the percentage of radiation reflected from the surface of the beams and launched

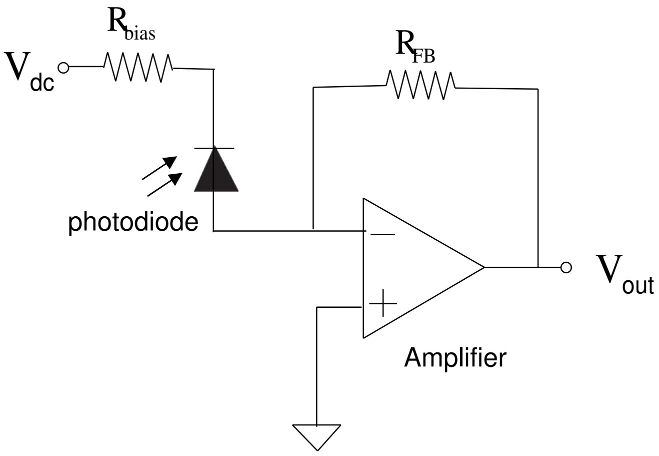

Figure 4.4: Simplified circuit diagram for amplification of the interferometer photodiode current

back into the fiber depends on the distance $d$ between the fiber and cantilever.

A photodiode followed by a transconductance amplifier is a typical circuit to measure the reflected light power. The diagram of the amplification of the interferometer photodiode current is shown in Figure 4.4. The signal voltage at the output of the photodiode is given by [28]

$$V_D = \eta R_{FB} P_D \tag{4.12}$$

where, $\eta$ is the responsivity of the photo detector and its value in our case is 0.8. $R_{FB}$ is the feedback resistor of the operational amplifier and its value shown in figure 4.4.

The photo detector output is connected to a Lock-in amplifier. Lock-in amplifier is a system which is designed for locking to a distinct frequency and measuring the amplitude and phase change at that reference. The lock-in instrument is intended for the detection and measurement of small periodic signals in the presence of high level of noise. It also enables one measure phase shifts and the harmonic contents of signals. Modern lock-in amplifiers can detect at several harmonics of the reference frequency (fundamental) in addition the fundamental frequency harmonic of the reference frequency.

A Labview program that performs the frequency scan and plots the magnitude

Table 4.1: The calculated and the measured values of the silicon nitride bridge and cantilevers

| Type | Length ($\mu m$) | Width ($\mu m$) | Thickness ($\mu m$) | $f_{cal}$ (kHz) | $f_{meas}$ (kHz) | Q | k (N/m) |
|---|---|---|---|---|---|---|---|
| Bridge | 400 | 5 | 0.5 | 26 | 20 | 40 | - |
| Cantilever | 250 | 30 | 2 | 41.97 | - | - | 0.8 |
| Cantilever | 200 | 30 | 2 | 65.57 | - | - | 1.5 |
| Cantilever | 150 | 30 | 2 | 116.58 | - | - | 3.7 |
| Cantilever | 100 | 30 | 2 | 262 | - | - | 12.6 |
| Cantilever | 50 | 30 | 2 | 1049 | - | - | 100.8 |

and the phase as a function of frequency was written . The Labview VI has a front panel control for the frequency step used in the scan, and has some control over the rate with which the scan is performed.

## 4.2 Fiber Optic Interferometric Measurement Results

The cantilevers and bridges are excited to the electrostatic excitation, the oscillation amplitudes are measured as a function of frequency of the excitation. The signal generator is connected to the Reference Input of the Lock-in Amplifier (SLS 830). This signal generator and the high voltage generator are adjusted to 1 V and 50 V, respectively to excite the beams. The mechanical resonances of the beams are determined by their geometry and their material properties such as density and elastic modulus. For calculated values, Young's modulus, $E$, and the density, $\rho$ is taken 210 GPa and 3184 $kg/m^3$ shown in Table 4.3, respectively. The calculated and measured results are shown in Table 4.1. In the case of a rectangular shape beams, many different resonance modes can exist, such as bending, twisting, expanding and contracting. In this study, we are only interested in observing the bending mode.

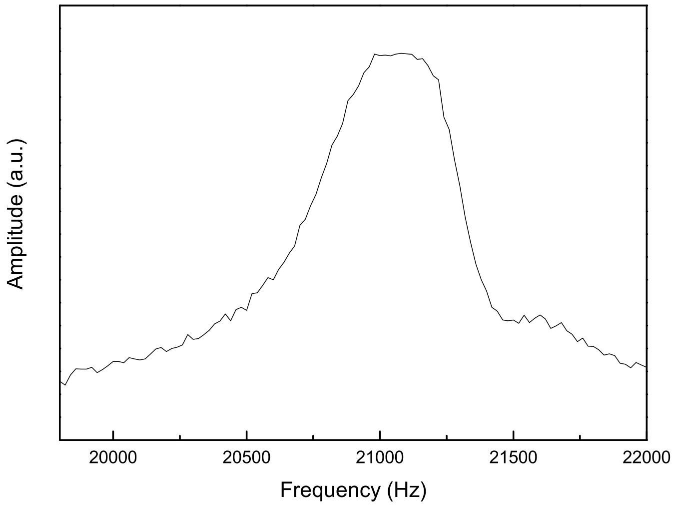

Figure 4.5: The amplitude versus frequency graph of the both side suspended oscillator beam, bridge#1

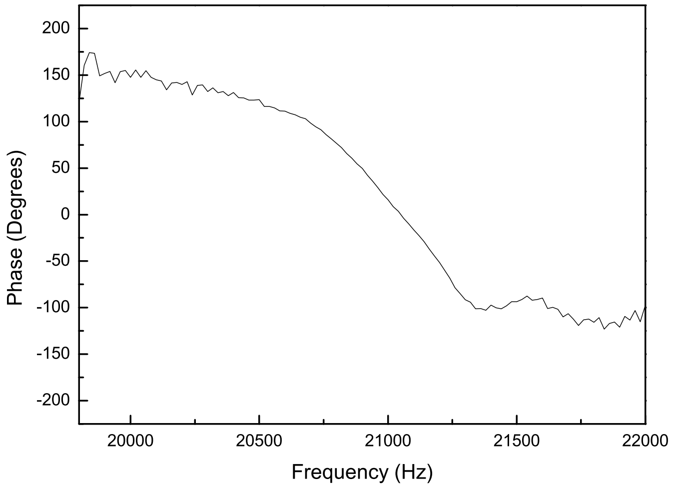

Figure 4.6: The phase versus frequency graph of the both side suspended oscillator beam, bridge#1

The mean separation between the reflectors, (cavity length), is adjusted by using the micropositioner. Photodetector output is connected to the oscilloscope. The results obtained by using this technique are shown in Figures 4.5, 4.6, 4.7, and 4.8.

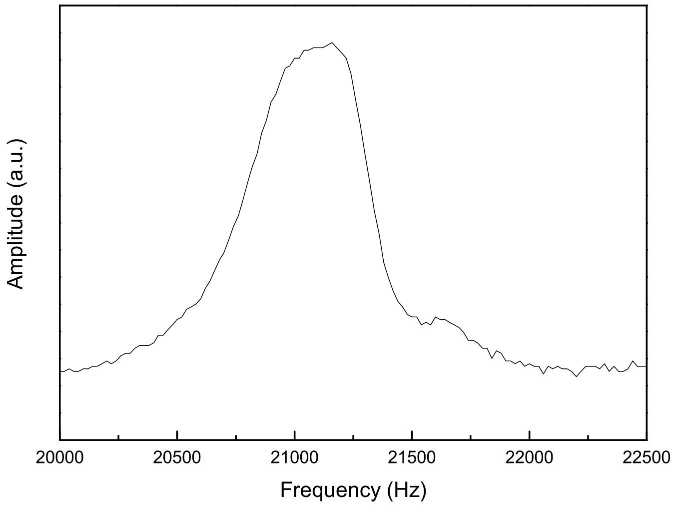

Figure 4.7: The amplitude versus frequency graph of the both side suspended oscillator beam, bridge#2

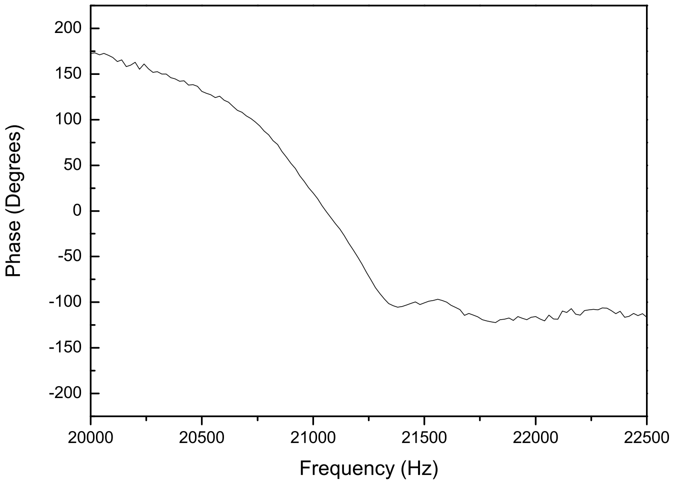

Figure 4.8: The phase versus frequency graph of the both side suspended oscillator beam, bridge#2

Figures 4.5, 4.6, 4.7, 4.8 give the magnitude and phase plot of the deflection as a function of the frequency. Note that at the resonance frequency, there is a sharp transition in the magnitude and phase of the output but at the same time. However, operating the systems at this resonance point enhances the sensitivity to ambient environmental parameters such as temperature, and pressure.

Operating at resonance is important for sensing, if the sensor comprises of elements that operate at their characteristic resonance and the effect of the measurement is detected as a slight change in the resonance characteristics of these elements. Resonant sensing generally involves the detection of the input measure by means of a resonance frequency shift in sensing device or amplitude or phase changes at constant excitation frequency.

## 4.3 Beam Deflection Atomic Force Microscopy

The microfabricated cantilever is mounted to the sample holder of the Nanosis beam deflection atomic force microscope head [31]. A conventional beam deflection method has been employed to measure the resonance frequency and and the phase change of the cantilever. The set-up used is shown in Figure 4.9.

In this method, the cantilever displacement is measured by detecting the deflection of a laser beam (650 nm laser diode) which is reflected off its backside. A schematic representation of this approach is shown in Figure 4.10 [32]. The sensitivity of the deflection set up is limited by mechanical vibration, the pointing stability of the laser and quadrant photo detector. This method enables the measurement of the cantilever displacement over a wide range of frequencies. Laser beam does not require a vacuum, it can be used with conductive and insulating samples, and it can be used with a variety of SPM modes.

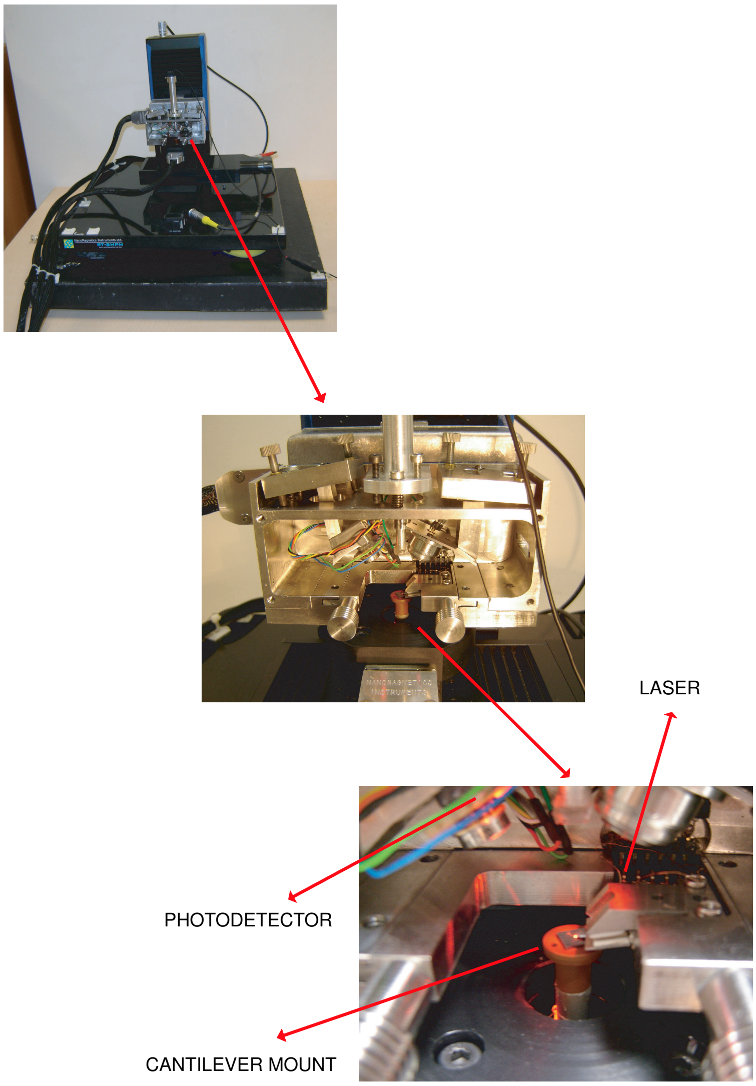

Figure 4.9: The view of the beam deflection AFM set up from NanoSis [31].

In this arrangement, a small deflection of the cantilever can tilt the reflected beam and change the position of the beam on the detector. Angular deflection of the cantilever causes a two-fold larger angular deflection of the laser beam. The reflected laser beam strikes a quadrant position-sensitive photodetector. A quadrant detector whose schematic view is given in Figure 4.11 is capable of measuring lateral displacement in two dimensions. The quadrant detector consist of four photodiodes (quadrants) positioned symmetrically around the center of the detector and separated by a narrow gap. The position information is derived from the optical signal powers received by the quadrants, the electrical contribution of which then serves to define the relative position of the light spot with respect to the center of the device. Calculation of the spot position is based on the subtracting the opposite signals in the direction of the measured axis and dividing this result by the sum of the same signals. The limits for the measurement accuracy are set by the achievable signal to noise ratio (SNR) and the reflector (here SOI cantilevers) background contrast, defined as the ratio of the powers of the signals received from the reflector and the illuminated background. The sum of these signals always yields the actual resonance frequency and phase change if a good feedback is provided.

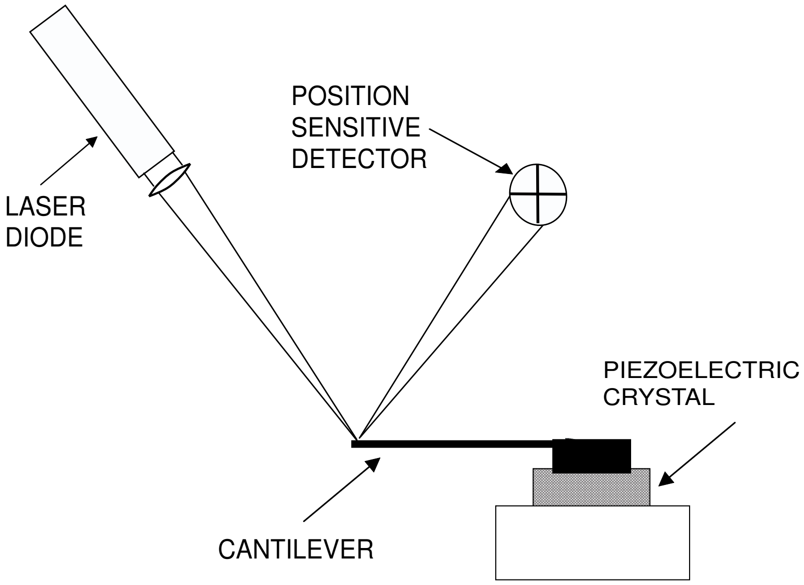

Figure 4.10: The schematic representation of the approach set up for deflection detection of SOI cantilevers

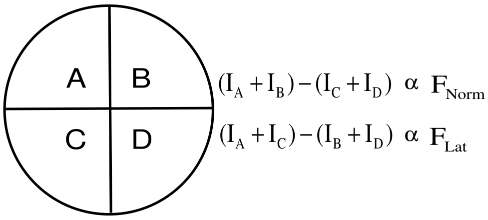

Figure 4.11: A quadrant phodetector

The SOI cantilevers whose resonance frequencies are given in Table 4.2 can reflect the laser beam back because of its material properties (that acts as a mirror at the laser wavelength). The properties of the reflectors determine the received signal level and the target background contrast. Then they have a considerable effect on the measurement accuracy.

The SOI cantilevers are actuated by using Phase-Locked Loop [33] as a signal generator connected to a piezoelectric element on which the cantilevers are mounted. When piezoelectric material are subjected to an externally applied voltage, they can change the shape by a small amount in every direction. The working principle of the piezoelectric materials is that they have two crystalline configurations. One structure is organized, while the other is not. Organization of the structure can be done with polarization of the molecules which make up the material. Hence, a non-polarized material has a non-organized structure, whereas the polarized material has organized structure. To polarize the material, voltage or electricity must be applied through it. As a result of this force, the molecules of the material reorient themselves, then changing the shape of the material.

By using this technique, with NanoMagnetics Instruments Atomic Force Microscope [31] and Phase-Locked Loop , we use the set up experiment shown in Figure 4.12. USB Phase-Locked Loop is used here as a signal generater only. PLL is basically a closed loop frequency control system. It is based on the phase sensitive detection of the phase difference between the input and output signals. In this system, PLL is used to drive an AC voltage to dither the piezo to oscillate the cantilevers mechanically and measures the response of the system by

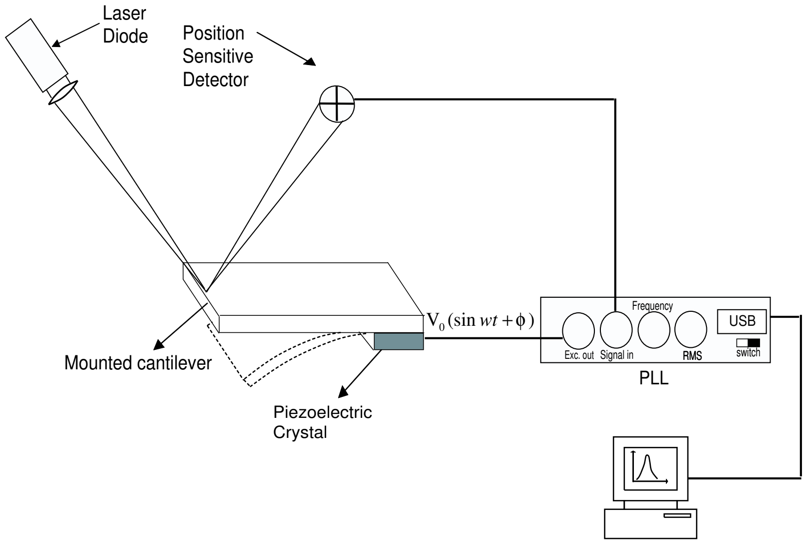

Figure 4.12: The schematic description of the beam deflection set up

measuring the signal generated by cantilevers. It also measures the phase change of the oscillation. The connection schematics is shown in the block diagram in Figure 4.12. It is also connected to a PC to monitor the resonance frequency, phase change and the quality factor of the cantilevers.

## 4.4 Beam Deflection Atomic Force Microscopy Results

The calculated and measured resonance frequency values of cantilevers using this techniques are shown in Table 4.2. For calculated values, Young‘s modulus, $E$, and the density, $\rho$ is taken 179 GPa and 2330 $kg/m^3$ shown in Table 4.3, respectively. The photograph of the SOI cantilevers measured by using this method are shown in Figure 3.7.

The measured resonance curve by this technique is shown in the Figures 4.13, 4.14 and 4.15 for SOI cantilevers listed in Table 4.2.

Figures 4.13, 4.14, and 4.15 are the experimentally measured plots of the power spectrum of the SOI cantilevers output over the different kHz range order

Table 4.2: The calculated and the measured parameters of the SOI cantilevers

| Type | Length ($\mu m$) | Width ($\mu m$) | Thickness ($\mu m$) | $f_{cal}$ (kHz) | $f_{meas}$ (kHz) | Q | k (N/m) |
|---|---|---|---|---|---|---|---|
| Cantilever | 140 | 50 | 4 | 288 | 272 | 562.0 | 52.1 |
| Cantilever | 180 | 50 | 4 | 174 | 165 | 398 | 24.0 |
| Cantilever | 240 | 50 | 4 | 98 | 91 | 370 | 10.3 |

Table 4.3: Density and Young's Modulus for Siliconnitride and Silicon

| Type | E (GPa) | $\rho$ ($kg/m^3$) |
|---|---|---|
| Siliconnitride | 210 | 3184 |
| Silicon | 179 | 2330 |

centered around the resonance frequency.

The cantilevers were designed with resonance frequencies lying between the 7 kHz to 1 MHz. However, in the etching step of the fabrication process, the SOI cantilevers are etched by using RIE, from the front side, then backside pattern is defined to etch the silicon from the backside. This alignment is not perfectly done because of the used Karl Suss Mask Aligner, KSM MJB 3 Mask Alignment and Exposure System (It has just only one side pattern definition, alignment feature). This result is seen in the Figure 3.7, then the cantilever's lengths were lower than the designed values. The calculated values shown in Table 4.2 are found using measured dimensions.

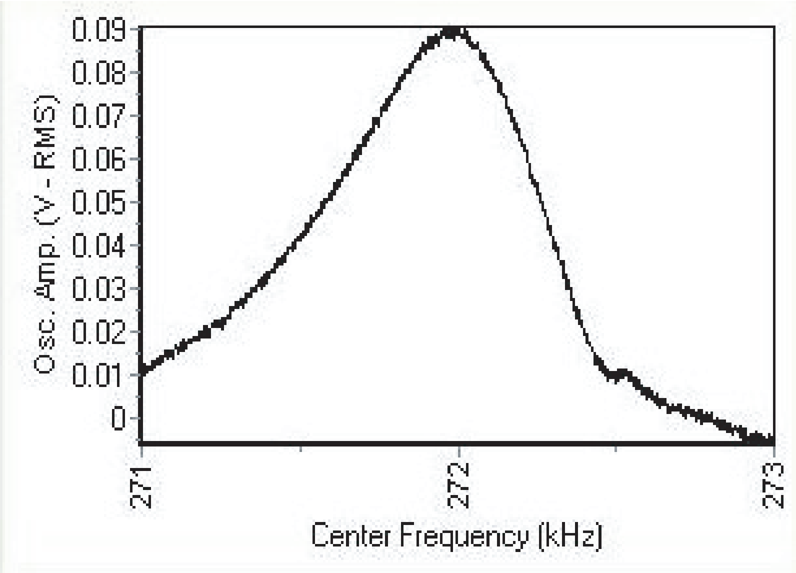

Figure 4.13: The measured resonance curve for SOI cantilever#1

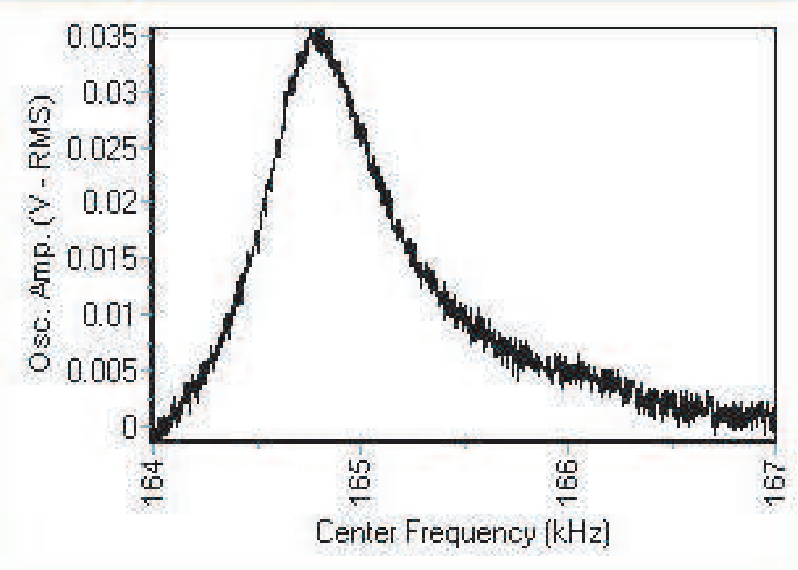

Figure 4.14: The measured resonance curve for SOI cantilever#2

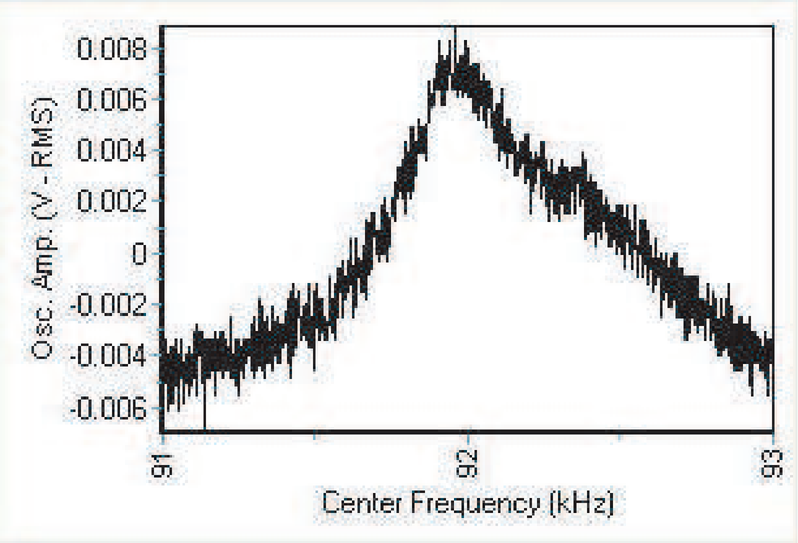

Figure 4.15: The measured resonance curve for SOI cantilever#3

# Chapter 5

# CONCLUSION

In this study, we developed processes leading to the fabrication of some basic MEMS devices namely cantilevers and beams. SOI AFM cantilever beams and silicon nitride cantilevers and bridges which are clamped from both ends were microfabricated.

We calculated analytically the physical parameters associated with these structures of different sizes, such as the natural resonance frequency of the oscillations. The characterization of the beams, cantilevers and bridges are discussed by using the fiber optic interferometric method and the beam deflection AFM method. First step, the fabrication of the devices are explained and then the resonance frequency curve and the quality factor of the bridges and the cantilevers are measured. The fabrication of the cantilevers and bridges are performed at the Advanced Research Laboratory of Physics Department at Bilkent University. The beam's fundamental resonance frequencies are designed in the 7.2 kHz to 1 MHz range for silicon nitride cantilevers, and from 15 kHz to 2 MHz for SOI cantilevers. However, in the fabrication process, all cantilevers designs were not successful mainly due to difficulties in KOH etching. The obtained resonance frequencies are shown in the Tables 4.1 and 4.2. It is seen that the calculated values of the resonance frequencies found by using the given equations in Chapter 2 are comparable to the measured values. The deviations may come from the loss mechanisms are discussed in the theory section or the material properties using for fabrication or inaccuracies in the measured dimension. The Young's modulus, refractive index and the density of silicon nitride thin film are generally different from the theoretical values taken by from literature. Since these parameters are effected by the growth process. The deviations may also come from the testing measurements. Since, Al coated cantilevers will be strained because of the deposition of the thin Al film. Then the Al thin film is removed. The removal of Al thin film reduced the reflection from the surface of the cantilever considerably. These problems result to the fact that the resonance frequency of the silicon nitride cantilevers are not measured.

# Bibliography

[1] A. A. Seshia, Integrated Micromechanical Sensors for Inertial Measurement Systems, PhD Thesis, University of California Berkeley, (2002).

[2] Chuanli Zhang, Guanshui Xu, Qing Jiang, Analysis of the Air-damping Effect on a Micromachined Beam Resonator, Mathematics and Mechanics of Solids, **8**, 315-325, (2003).

[3] Franz J. Giessibl, Advances in atomic force microscopy, Reviews of Modern Physics, **75** (3), (2003).

[4] F. J. Giessibl, A direct method to calculate tip-sample forces from frequency shifts in frequency-modulation atomic force microscopy, Applied Physics Letters, **78** (1), (2001).

[5] K. L. Ekinci, Y. T. Yang, M. L. Roukes, Ultimate limits to inertial mass sensing based upon nanoelectromechanical systems, Journal of Applied Physics, **95** (5), (2004).

[6] S. M. Hutcherson, Theoretical and Numerical Studies of the Air Damping of Microresonators, MS Thesis, Georgia Institute of Technology, (2004).

[7] K. L. Ekinci, X. M. H. Hung, M. L. Roukes, Ultrasensitive nanoelectromechanical mass detection, Applied Physics Lettes **84** (22), (2004).

[8] M. Tortonese, R. C. Barrett, C. F. Quate, Atomic resolution with an atomic force microscope using piezoresistive detection, Applied Physics Letters, **62** (8), (1993).

[9] P. G. Datskos, T. Thundat, Nickolay V. Lavrik, Micro and Nanocantilever Sensors, Encyclopedia of Nanoscience and Nanotechnology, Volume X: pages 1-10.

[10] Goran Stemme, Resonant Silicon Sensors, J. Micromech. Microeng., **1**, 113-115 (1991).

[11] Jin Qui, Jeffrey H. Lang, Alexander H. Slocum, A Curved-Beam Bistable Mechanism, Journal of Microelectromechanical Systems, **13** (12), (2004).

[12] K. Peterson, Silicon as a Mechanical Material, Proceedings of the IEEE., **70** (5), 420-457 (1982).

[13] L. Meirovitch, Fundamentals of Vibrations, New york: McGraw Hill, (2001).

[14] M. Duemling, Modeling and characterization of nanoelectromechanical systems, MS. Thesis, Virginia Polytechnic Institute and State University, (2002).

[15] James M. Gere, Stephen P. Timeshenko, Mechanics of Materials, 2nd Edition, PWS-KENT Publishing Company, Boston.

[16] A. A. Shabana, Vibration of Discrete and Continous systems, Springer-Verlag, (1997).

[17] F.R. Blom, S. Bouwstra, M. Elwenspoek, J.H.J. Fluitman. Dependence of the quality factor of micromachined silicon beam resonators on pressure and geometry, J, Vac. Sci. Technol. **B**10 (1), (1992).

[18] Newell, W.E. Miniaturization of tuning forks, Science, **161**, 1320-1326 (1968).

[19] Y.H. Cho, A.P. Pisano, R.T. Howe, Viscous Damping Model for Laterally Oscillating Microstructures, J. Microelectromech. Syst., **3** (81), (1994).

[20] L. Sekaric, D.W. Carr, S.Evoy, Nanomechanical resonant structures in silicon nitride:fabrication, operation and dissipation issues, Sensors and Actuators A **101**, 215-219, (2002).

[21] J. Yang, T. Ono, M. Esashi, Surface effects and high quality factors in ultrathin single-crystal silicon cantilevers, Applied Physics Letters, **77** (23), (2000).

[22] W. A. Zdaniewski, G. E. Rindone, D. E. Day, J. Mater. Sci., **14**, 763 (1979).

[23] D. Bilic, Micromachined resonators, PhD. Thesis, University of California Berkeley, 2001.

[24] C. Wong, K. Wang, C. Nguyen, VHF Free-Free Beam High-Q Micromechanical Resonators, Journal of Microelectromechanical Systems, **9** (3), (2000).

[25] R. Lifshitz, M. L. Roukes, Thermoelastic damping in micro and nanomechanical systems, Phys. Rev. B **61** (8), (2000).

[26] B. H. Houston, D. M. Photiadis, M. H. Marcus, J. A. Bucaro, Xiau Liu, J. F. Vignola, Thermoelastic loss in microscale oscillators, Applied Physics Letters, **80** (7), (2002).

[27] Nadim Maluf, An Introduction to Micromechanical Systems Engineering (Artech House Boston, London, 2000).

[28] Aykutlu Dâna, Electrostatic Force Spectroscopy of Near Surface States, PhD Thesis, Stanford University, (2004).

[29] D. Rugar, H. J. Mamin, P. Guether, Improved fiber-optic interferometer for atomic force microscopy, Applied Physics Letters, **55** (25), (1989).

[30] D. Rugar, P. Hansma, Atomic Force Microscopy, Physics Today, **11**, 23, (1990)

[31] NanoSis Instuments Ltd. Cyberpark, Cyber Plaza B. Blok No:207/3, Bilkent, Turkey.

[32] G. Meyer, Nabil M. Amer, Novel Optical approach to atomic force microscopy, Applied Physics Letters, **53** (12), (1988).

[33] Nanomagnetics Instuments Ltd. Cyberpark, Cyber Plaza B. Blok No:207/2, Bilkent, Turkey, www.nanomagnetics-inst.com